Biophysical Journal
Article

Biophysical Society

Endoplasmic reticulum network heterogeneity guides diffusive transport and kinetics

Zubenelgenubi C. Scott,[1] Katherine Koning,[2] Molly Vanderwerp,[2] Lorna Cohen,[3] Laura M. Westrate,[2] and Elena F. Koslover[1,*]

[1]Department of Physics, University of California, San Diego, La Jolla, California; [2]Department of Chemistry and Biochemistry, Calvin University, Grand Rapids, Michigan; and [3]Van Andel Institute, Grand Rapids, Michigan

ABSTRACT The endoplasmic reticulum (ER) is a dynamic network of interconnected sheets and tubules that orchestrates the distribution of lipids, ions, and proteins throughout the cell. The impact of its complex, dynamic morphology on its function as an intracellular transport hub remains poorly understood. To elucidate the functional consequences of ER network structure and dynamics, we quantify how the heterogeneity of the peripheral ER in COS7 cells affects diffusive protein transport. In vivo imaging of photoactivated ER membrane proteins demonstrates their nonuniform spreading to adjacent regions, in a manner consistent with simulations of diffusing particles on extracted network structures. Using a minimal network model to represent tubule rearrangements, we demonstrate that ER network dynamics are sufficiently slow to have little effect on diffusive protein transport. Furthermore, stochastic simulations reveal a novel consequence of ER network heterogeneity: the existence of "hot spots" where sparse diffusive reactants are more likely to find one another. ER exit sites, specialized domains regulating cargo export from the ER, are shown to be disproportionately located in highly accessible regions, further from the outer boundary of the cell. Combining in vivo experiments with analytic calculations, quantitative image analysis, and computational modeling, we demonstrate how structure guides diffusive protein transport and reactions in the ER.

SIGNIFICANCE The endoplasmic reticulum (ER) is the largest organelle in the eukaryotic cell, forming a web of interconnected hollow tubules and sheets. The ER is central to the transport of many cellular components such as lipids, ions, and proteins. However, the impact of the ER's complex network architecture on these transport processes remains opaque. Using live-cell experiments and simulations, we demonstrate that structural heterogeneity leads to nonuniform transport of proteins to nearby regions of the ER. As a consequence, certain regions of the network function as "hot spots" where diffusive reactants are more likely to find each other. In live cells, sites of protein export are preferentially localized to regions of greater accessibility.

INTRODUCTION

The eukaryotic cell contains myriad complex structures and compartments, each serving a specialized functional role. These include the tortuous interior of interconnected mitochondria (1), the stacked sheets (2) and tubular networks (3,4) of the perinuclear and peripheral endoplasmic reticulum (ER), and the intertwined actin and microtubule networks of the cytoskeleton (5–7). The morphology of these intracellular structures modulates the long-range active and passive transport of particles within them (8). For example, the winding cristae of mitochondria slow down the long-range spread of particles (1), whereas spiral dislocations connecting ER sheets facilitate more rapid diffusive transport (2,9).

A number of theoretical studies have demonstrated that the architecture of the domain can play an important role in determining reaction rates, a general phenomenon described as "geometry-controlled kinetics" (10). Emergent kinetic behaviors such as ultrasensitivity, bistability, and proofreading can be promoted or suppressed when enzyme and reactant diffusion is perturbed by crowding or by association with cellular structures (11–13). Additional effects arise when the domain structure is dynamic, leading to time-varying effective diffusivity (14,15) and broadening the distribution of search times (16).

One important class of intracellular geometries includes network structures, consisting of effectively one-dimensional

Submitted February 9, 2023, and accepted for publication June 28, 2023.

*Correspondence: ekoslover@uscd.edu

Editor: Alexander Fletcher.

https://doi.org/10.1016/j.bpj.2023.06.022

edges connected at junction nodes. The transport properties of spatial networks (17) have been studied in a variety of contexts, from porous media (18) to neuronal maintenance (19,20). For instance, particles diffusing through networks of tubes and containers have been shown to exhibit novel transport properties such as wavelike concentration fluctuations (21), as well as enhanced reaction rates (22).

The peripheral ER (23–25) and the mitochondrial networks of yeast and mammalian cells (26,27) can both be described as spatial networks of interconnected hollow tubules. Studies of search kinetics in these networks have highlighted the importance of network connectivity, as described by the number of loops within the network (26,28). The connectivity of the organelles can be biologically perturbed by mutations in ER morphogens (3,25) and mitochondrial fusion and fission proteins (26,27). Prior studies have focused largely on global network architecture and transport properties, such as mean first-passage times (MFPTs) averaged over the entire network. Cellular networks, however, are not homogeneous lattices, implying that a significant amount of variability should be expected in local transport to specific regions (29). This variability has the potential to modulate encounter kinetics and dispersal to different regions of the cell.

The dynamic, interconnected web of the ER plays an important biological role as a delivery network for proteins, ions, and lipids throughout the cell (30–33). For example, phospholipids manufactured in the ER must diffuse through its membrane to contact sites with lipid droplets, mitochondria, and other organelles in order to be transferred to their eventual cellular destinations (33,34). Additionally, alteration of network structure through modulating expression of ER morphogens has been shown to affect the magnitude of calcium release, possibly due to altered transport through the ER lumen (30).

The ER also serves as a quality control hub for newly synthesized proteins destined for secretion (35,36). These proteins are co- or posttranslationally inserted into the ER lumen or membrane, interact with a variety of ER-resident chaperones to ensure correct folding, and exit the organelle after encountering one of several ER exit sites (ERES). The ERES are punctate, persistent structures that package secretory cargo into coat protein complex II (COPII)-coated vesicles for subsequent transport to the Golgi apparatus (37–40). While they are in the ER, the proteins targeted for secretion engage in diffusive transport to encounter their chaperone binding partners and to find the exit sites. Furthermore, certain steps in the protein quality control pathways are thought to occur in specialized local regions of the ER (41,42), necessitating transport of proteins into and out of these regions. Given that many of the biological functions of the ER rely on its ability to serve as a topologically isolated transport network throughout the cell, understanding how network architecture modulates particle transport and encounter kinetics forms an important problem in cell biology.

In this work, we focus on the spatial heterogeneity of the peripheral ER network in mammalian (COS7) cells. We demonstrate that structural variability across individual ER networks translates to heterogeneous diffusive accessibility for different ER regions within the same cell. Live-cell imaging data is used to show that locally photoactivated membrane proteins spread nonuniformly to nearby regions of the ER, in agreement with simulation results that predict preferential transport to better-connected regions of the network. The contribution of dynamic ER network rearrangements is quantified using a minimal network model (23,43) and shown to have little effect on membrane protein spreading. Furthermore, with the aid of stochastic simulations, we demonstrate that the heterogeneity of the ER leads to the formation of "hot spots" where diffusing reactants are more likely to find each other. In live cells, we additionally find that ERES are preferentially localized to regions of higher accessibility as dictated by network connectivity and proximity to the perinuclear region. By examining the impact of ER network heterogeneity on diffusion-limited reactions and local protein spread, this work sheds light on the structure-function relationship of a biologically crucial organelle.

MATERIALS AND METHODS

DNA plasmids

ER plasmids (mCherry_KDEL, KDEL_Venus or BFP_KDEL) were described previously (44–46). Plasmids expressing fluorescently tagged COPII proteins GFP_Sec16s, GFP_Sec23A, GFP_Sec24D, and EYFP_Sec31A were acquired from addgene (gifts from Benjamin Glick #15775, David Stephens #66609 and #66613, Henry Lester #32678) (47–49). Generation of PAGFP_Calnexin was performed by PCR amplification of calnexin from mEmerald_Calnexin (gift from Michael Davidson, addgene #54021) using iProof high-fidelity DNA Master mix (Bio-Rad) and primers flanked with Xho1 or BamH1 recognition sites (Primer Fwd: 5′-AGATCTCGAGCTCATGGAAGGGAAGTG GTTGCTG -3′ and Primer Rev: 5′-CCGATGGATCCCGCTCTCTTCGT GGCTTTCTGTTTCT-3′) according to manufacturer instructions. Amplified DNA was purified using the Monarch Gel Extraction Kit (New England Bioscience) according to manufacturer protocol and digested with Xho1 and BamH1 (NEB). The digested calnexin was then ligated into PAGFP_N1 (gift from Jennifer Lippincott-Schwartz, addgene #11909) (50) using T4 DNA ligase (NEB) according to manufacturer protocol. Bacterial clones were screened for insertion of calnexin sequence and confirmed by sequencing.

Photoactivation experiment

COS7 cells were purchased from ATCC and cultured in Dulbecco's modified Eagle's medium (DMEM) supplemented with 10% fetal bovine serum and 1% penicillin/streptomycin. For all imaging experiments, COS7 cells were seeded in six-well, plastic-bottom dishes at 7.5×10^4 cells/ml about 16 h before transfection. Plasmid transfections were performed using lipofectamine 3000, as described previously (51). The following standard DNA amounts were transfected per mL: 0.2 μg mCherry_KDEL, 0.2 μg BFP_KDEL, and 0.4 μg PAGFP_Calnexin. Cells were transferred to 35-mm imaging dishes (CellVis) at least 16 h before imaging.

All photoactivation experiments were performed at the Van Andel Institute Optical Microscopy Core on a Zeiss LSM 880, equipped with an Axio Observer 7 inverted microscope body, stage surround incubation, Airyscan detector, two liquid-cooled MA_PMT confocal detectors, and one 32-channel

GaAsP array confocal detector. Images were acquired with a Plan-Apochromat 63x (NA 1.4) oil objective with 3x optical zoom using Zeiss Zen 2.3 Black Edition software. Photoactivated target regions of interest (60 x 60 pixels) in the peripheral ER network were stimulated with 405-nm light (single pass with 0.51 μsec pixel dwell) to selectively activate defined regions within the peripheral ER. Cells were tracked for at least 2 min after stimulation with constant acquisition (0.629 s/frame) to track diffusion of photoactivated signal into the surrounding ER network.

Image analysis and network structure extraction

The machine learning segmentation toolkit ilastik (52) was employed to segment ER network structures from live-cell images using the mCherry_KDEL marker. A custom-written skeleton tracing subroutine in MATLAB (53) was used to extract a network structure from the probability file output by ilastik. This code is publicly provided at https://github.com/lenafabr/networktools and includes data structures for storing the network morphology as a set of nodes connected by edges with curved spatial paths. The networks were manually curated (using a network editing GUI provided as part of the networktools package) to remove unphysical terminal nodes arising from skeletonization artifacts. Compact circular regions were cut out from the extracted networks for statistical analysis of local edge length, global mean first passage times, and pair-wise reaction times.

Mean first-passage times on tubular and reservoir networks

In our base model, MFPTs are computed on networks consisting of edges joined at point-like nodes. Details of the computation are outlined in Ref. (29). In short, we find the splitting probability P_{ik} and waiting time Q_i for a diffusive particle starting at node i to first reach neighboring node k:

$$P_{ik} = \frac{1/l_{ik}}{\sum_{j=1}^{d_i} 1/l_{ij}}, \; Q_i = \frac{1}{2D}\frac{\sum_{j=1}^{d_i} l_{ij}}{\sum_{j=1}^{d_i} 1/l_{ij}}. \quad (1)$$

Here, d_i is the node degree, and l_{ik} is the length of the connecting edge, and D is the particle diffusivity. The MFPT from node i to a target node is then given by the following (29):

$$\tau_i = \left[(\mathbf{I} - \mathbf{P})^{-1}\cdot\mathbf{Q}\right]_i, \quad (2)$$

where $\mathbf{I}$ is the identity matrix, and the matrix and vector $\mathbf{P}, \mathbf{Q}$ are defined by Eq. 1, with the row and column corresponding to the target removed. The global mean first-passage time (GMFPT) is defined as the MFPT to a given target k, averaged over all starting nodes i.

In this work, we also introduce a novel extension to the base model that allows calculation of search times on networks with enlarged nodes or "reservoirs" (details in supporting material, Section S2). The model represents the motion of particles between disk-shaped reservoirs and connecting tubules as transitions between distinct spatial states. Waiting times for transition out of the reservoir are set by two-dimensional diffusive escape into the narrow tube entrances. The additional states associated with trapping in the reservoirs are included in the transition matrix $\mathbf{P}$ and waiting time vector $\mathbf{Q}$ to compute the MFPTs according to Eq. 2.

We consider two extended network models. In supporting material, Fig. S3, we randomly select nodes to be expanded into larger reservoirs. GMFPTs are computed to both the point-like remaining nodes of the network and to a central target inside each reservoir, where the radius of the target is equal to the network tubule radius. Particles are assumed to start on the nodes, in proportion to the node area. When computing first passage times on a network with observed exit site positions, we introduce a single, large, disk-like reservoir representing the perinuclear region. GMFPTs are computed for particles starting uniformly distributed along the network edges and the reservoir, in proportion to the associated surface area for the tubules and the disk. Details for computing MFPTs for a particle starting on a network edge can be found in Ref. (29).

Analysis of photoactivated spreading data

Imaging datasets for nine individual cells are selected for analysis, each of which has a photoactivation region surrounded by a well-defined tubular network structure with primarily three-way junctions. The net signal over time is computed in 10 distinct wedge regions comprising an annulus around the photoactivation region with inner radius 3.5 μm and outer radius 6 μm. The photoactivated signal in wedge j at time i is defined as w_{ij}^{PAGFP}. The fractional signal is then given by $f_{ij}^{\mathrm{PAGFP}} = w_{ij}^{\mathrm{PAGFP}}/P_0^{\mathrm{PAGFP}}$ where P_0^{PAGFP} is the total initial signal within the photoactivated zone. We find the slope ("signal arrival rate") of the fractional signal via a linear fit over the first 10 s of imaging time after photoactivation.

Two rounds of filtering are applied to ensure a meaningful relationship between the photoactivated signal dynamics and the observed network structure. The first filter removes regions with extremely rapid and/or large fluctuations in the ER signal. We calculate the time-variance in the fractional signal in each wedge as

$$V_j = \mathrm{var}_i\left(w_{ij}^{\mathrm{PAGFP}} \Big/ m_i^{\mathrm{PAGFP}}\right), \quad (3)$$

where $m_i^{\mathrm{PAGFP}} = \sum_j w_{ij}^{\mathrm{PAGFP}}$ is the total signal in the annular region at time i. Given the distribution of these time-variances, a threshold of $2.5 \times (\mathrm{MAD} \times 1.4826)$, where MAD is the median absolute deviation, is used to define outliers with extreme ER dynamics, in keeping with commonly used outlier detection methods (54).

The second round of filtering removes instances where network extraction does not accurately capture the underlying ER morphology. For example, small peripheral sheet regions, expanded junctions, or dense tubular matrices (4) can complicate the extraction of a well-defined network structure. Outlier regions are defined as those where the extracted total tubule length and the ER marker (mCherry_KDEL) signal levels are mismatched. Specifically, we compute the time-averaged fractional mCherry_KDEL signal for each wedge region in each cell as $s_j = \langle w_{ij}^{\mathrm{mCherry}}/m_i^{\mathrm{mCherry}}\rangle_i$. A linear fit is performed relating s_j with the total extracted network length for each wedge, averaged over time. Any wedge with a residual above $2.5 \times (\mathrm{MAD} \times 1.4826)$ is filtered out of the analysis. Wedge regions filtered out due to either criterion are shown as gray dots in statistical plots.

Simulations of photoactivation on static networks

For each frame in a photoactivation video, the ER network structure is extracted from the mCherry_KDEL fluorescence channel, as described in the image analysis and network structure extraction section. On each individual network structure, simulations of diffusing particles are conducted via a kinetic Monte Carlo method, as described in prior work (29). Briefly, analytically computed propagator functions are used to sample the time required for each particle to transition between neighboring nodes and edges, obviating any artifacts associated with a fixed time discretization. This method allows the particle to propagate in larger timesteps than would be achievable through classic Brownian dynamics simulations on a network.

Batches of $N = 10,000$ particles are initiated within the experimentally photoactivated region, a 3×3 μm patch in the peripheral ER. Particles propagate through the network with a diffusivity of $D = 1\ \mu\mathrm{m}^2/\mathrm{s}$, consistent with previous measurements of ER membrane protein diffusivity (24). All particle positions are saved at a frame rate matching the experimental imaging rate, $dt = 0.629$ s.

To process the simulated data, we define individual wedge regions of the same size and location as in the experimental images and analyze the number of particles in each. Note that each simulation is run on a static network

extracted from a single frame (k) of the experimental image. The simulated signal in each wedge (w_{kij}^{sim}) is then defined as the total number of particles in wedge j and time point i on the network extracted from frame k, and the fractional signal is $f_{kij}^{\mathrm{sim}} = w_{kij}^{\mathrm{sim}}/N$.

We next average this fractional signal over the different networks, defining $f_{ij}^{\mathrm{sim}} = \langle f_{kij}^{\mathrm{sim}} \rangle_k$ (see supporting material, Fig. S2 *A*.iii for example averaged signal versus time curves). The resulting values are used to find the signal arrival rate (slope over first 10 s), exactly as for experimental data. Alternative methods for incorporating the time-varying ER network structure are considered in the supporting material.

The simulations make it possible to incorporate a range of values for the particle diffusivity. We accomplish this by rescaling the simulation time in our analysis, which leads to a rescaling of the diffusivity (assuming static networks). For example, to test whether $D_{\mathrm{eff}} = 0.5\ \mu\mathrm{m}^2/\mathrm{s}$ is a better representation of the protein diffusivity than $D_{\mathrm{orig}} = 1\ \mu\mathrm{m}^2/\mathrm{s}$, we can find the slope of f_{ij}^{sim} over time $T_{\mathrm{scale}} = \frac{D_{\mathrm{eff}}}{D_{\mathrm{orig}}} \times 10\mathrm{s} = 5$ s. The slope is then multiplied by $\frac{D_{\mathrm{orig}}}{D_{\mathrm{eff}}}$ to arrive at a simulated arrival rate with an effective diffusivity of $D_{\mathrm{eff}} = 0.5\ \mu\mathrm{m}^2/\mathrm{s}$.

We perform a linear fit of the rescaled simulated rates to the experimental protein arrival rates (slopes over 10 s). Repeating over a range of effective diffusivities, the value of D_{eff} with the optimal fit indicates the best estimate of ER membrane protein diffusivity given the photoactivated spreading data.

Minimal model for dynamic ER networks

To estimate the effects of ER network rearrangements on particle spreading, we conduct Brownian dynamics simulations on synthetic dynamic networks. To represent the dynamic network, we use a modified version of the previously published "minimal network model" (23,43). In this model, the network consists of mobile nodes connected by edges, where the node positions $\mathbf{x}_i(t)$ obey an overdamped Langevin equation:

$$\frac{d\mathbf{x}_i}{dt} = -b\nabla f(\mathbf{x}_i) + \sqrt{2D_n}\boldsymbol{\eta}(t), \tag{4}$$

where $D_n \approx 10^{-3}\ \mu\mathrm{m}^2/\mathrm{s}$ (23) is the node diffusivity, b is the node mobility in units of μm/s, and $f(\mathbf{x}_i)$ is the total edge length attached to each node. Specifically, $f(\mathbf{x}) = \sum_{j=1}^{d} |\mathbf{x} - \mathbf{y}_j|$, where the sum is over neighbor nodes, and $\mathbf{y}_j$ are the neighbor positions. The stochastic variable $\boldsymbol{\eta}(t)$ is a Gaussian distributed noise term with mean zero and standard deviation 1. This model represents a network of edges that are under a constant tension, driving a minimization of their length.

As the edges of the network shrink, neighboring nodes approach each other. When two nodes are sufficiently close together, topological rearrangements of network connectivity can occur. If the two nodes are both degree 3 junctions, they undergo a T1 rearrangement (55) if and only if this decreases the total edge length. If one of the nodes has degree 2, or if they are connected by two edges (forming a short loop), then the two nodes can fuse together into a single node. The combination of these processes allows for ring-closure events, as observed in live-cell imaging of ER dynamics (32,56).

To maintain a steady-state network structure, new edges are generated by a tube spawning and growth process. A new tube spawns at a fixed growth rate per existing total edge length (k, units of $\mathrm{s}^{-1}\mu\mathrm{m}^{-1}$). The new tube location is uniformly selected along existing edges. The nascent tube grows at a right angle from the parent edge, with fixed velocity $v = 2\ \mu\mathrm{m/s}$, comparable to rapid rates observed in dynamic ER images (40,57). When the tip of a nascent tube crosses an existing tube, it stops growing and fuses to form a new junction node.

Similar to (43), the balance between new tubule growth and shrinking due to length minimization enables the dynamic network to reach a stable steady state. Of the parameters in the model, the diffusivity is sufficiently low ($D \ll vl$, where $l \approx 1\ \mu\mathrm{m}$ is the characteristic edge length) to have little effect on network structure. Additionally, the tubule growth speed ($v \gg b$) is high enough that newly spawned tubules fuse much quicker than the node rearrangement timescales. The network structure is thus largely determined by the remaining two parameters k, b, which are set to match observations of COS7 ER in live-cell images.

The approximate growth rate k is extracted from videos of COS7 peripheral ER, labeled with 0.2 μg KDEL_Venus (transfected as described above) and imaged on the Zeiss LSM 880 at a frame rate of 0.315 s, by manually counting new growth events (Video S3). The number of growth events in a region of size 10 μm × 10 μm is manually counted over time interval 63 s. This number is normalized by the time interval and the time-averaged total segmented ER length within the region, giving: $k \approx 0.005\ \mu\mathrm{m}^{-1}\mathrm{s}^{-1}$.

Dimensional analysis indicates that the average steady-state edge length in the network scales as $l \sim \sqrt{b/k}$. We tune the node mobility b to set a typical ER network edge length $l \approx 1\ \mu\mathrm{m}$ (24), corresponding to an estimate of $b = 0.05\ \mu\mathrm{m/s}$.

The resulting dynamic network model thus has tubule lengths and turnover timescales that approximately represent those of the COS7 ER ("normal ER model"). For comparison, we consider also a model where b and k are both increased by twofold, allowing for more rapid turnover but the same steady-state structure ("fast ER model").

Simulating photoactivated spread on the dynamic network model

Diffusive particles ($N = 10,000$) are simulated on the dynamic network using Brownian dynamics, with particles moving along the network edges in discrete timesteps $dt = 10^{-3}$ s, with diffusivity $D = 1\ \mu\mathrm{m}^2/\mathrm{s}$ and network structure updated at each timestep. After each network update, the particle position is projected to the closest location in the new network. The network architecture is first evolved for a total time of 1000 s to allow it to reach steady state before initiating the diffusive particles. The particles are placed within a square 3 μm × 3 μm region of the network, and the joint simulations of particle and network evolution then proceed for an additional 15 s of simulated time.

The number of particles arriving in each wedge region surrounding the starting center is analyzed on both the dynamically evolving network and on each individual static network structure extracted at 0.6-s intervals from the simulation. The signal arrival rates are obtained as described in the previous section.

Paired particle simulations

Simulations of reactive particle pairs are run using the propagator-based approach, which enables particles to hop rapidly from node to node of the network until they come within the same neighborhood of each other. Details of the methodology, including the appropriate propagator functions for two reactive particles on the same edge, are provided in prior work (29). Each simulation is run until the two particles encounter each other, and the reaction position on the network is recorded. A total of $N = 1.6 \times 10^4$ particles are simulated on each network structure.

Two other families of network are also analyzed. Eight circular honeycomb networks are generated, each with the same diameter (18 μm) and total edge length as one of the eight ER structures analyzed. Mikado networks are generated by scattering N_{rod} randomly oriented rods of length L_{rod} in a square of size L_{space} x L_{space}. The intersections of these rods define the nodes of the network, and the segments of rods between intersections define the edges of the network. This algorithm generates highly heterogeneous networks with a density that is tunable by changing any of the three input parameters (58). However, Mikado networks tend to have degree 4 junctions, whereas ER (and honeycomb) networks are composed of mostly degree 3 junctions. Our modification to the Mikado networks is thus to remove

degree 4 nodes by iteratively removing one random edge from a randomly chosen degree 4 node until all nodes in the network have degree 3 or less. The Mikado parameters are chosen to be $N_{rod} = 80$, $L_{rod} = 12\ \mu$m, and $L_{space} = 24\ \mu$m, and a circular portion of the network is extracted with diameter 18 μm m, matching the circular ER networks. We generate many copies of these circular modified Mikado networks and select for analysis only those that have a total length within 5% of the corresponding ER network.

ERES localization on ER network

COS7 cells were seeded in plastic six-well dishes and transfected as described in the photoactivation experiment section. Cells were then imaged as previously described (40). The following standard amounts of DNA were transfected per mL: 0.1 μg GFP_Sec16s, 0.1 μg GFP_Sec23a, 0.1 μg GFP_Sec24d, 0.1 μg EYFP_Sec31a, and 0.2 μg mcherry_KDEL. Images were acquired on an inverted fluorescent microscope (TE2000-U; Nikon) equipped with a 100x oil objective (NA 1.4) on an electron-multiplying charge-coupled device camera (Andor). Live-cell imaging was performed at 37°C after media change to prewarmed imaging media (fluorobrite DMEM (Invitrogen) + 10% fetal bovine serum).

Images of 22 different COS7 cells are analyzed as described in the image analysis and network structure extraction section to extract the peripheral ER network structure. The perinuclear region is manually excised from each one. ERES locations are identified as puncta in the GFP or EYFP fluorescent signal using a previously published implementation of the standard particle localization algorithm by Crocker and Grier (59,60). We identify a total of 1443 peripheral and 2327 perinuclear ERES. The peripheral puncta are projected onto the nearest point along the extracted network structure.

To convert these structures into reservoir networks (model described in supporting material, Section S2), the centroid of the nodes bounding the excised perinuclear region is set to be the center of the reservoir. The average distance of the bounding nodes to the centroid determines the radius of the reservoir, R_+. Each bounding node is then connected to the reservoir via a tubule of length equal to the mean edge length of the network.

The GMFPT to each projected ERES is computed for particles starting uniformly distributed across the network. For comparison, an equivalent number of target points are selected uniformly at random along the edges of each network structure, and the GMFPT is computed to each of those points individually.

RESULTS AND DISCUSSION

ER network structures exhibit spatially heterogeneous accessibility

The peripheral ER forms an intricate web of tubules, with primarily three-way junctions scattered at varying densities across the cell periphery. We aim to characterize the heterogeneity of the network structure and its effects on the accessibility of different regions by particles diffusing on the network.

ER network morphologies are extracted from confocal images of the peripheral ER in cultured COS7 cells (Fig. 1 *A*), where these network structures are largely planar. The network structure is simplified into effectively one-dimensional edges (not necessarily straight), connected at point-like nodes. Although more complex peripheral structures, including hole-studded sheets (61) and dense localized matrices (4), have been observed, we focus here on

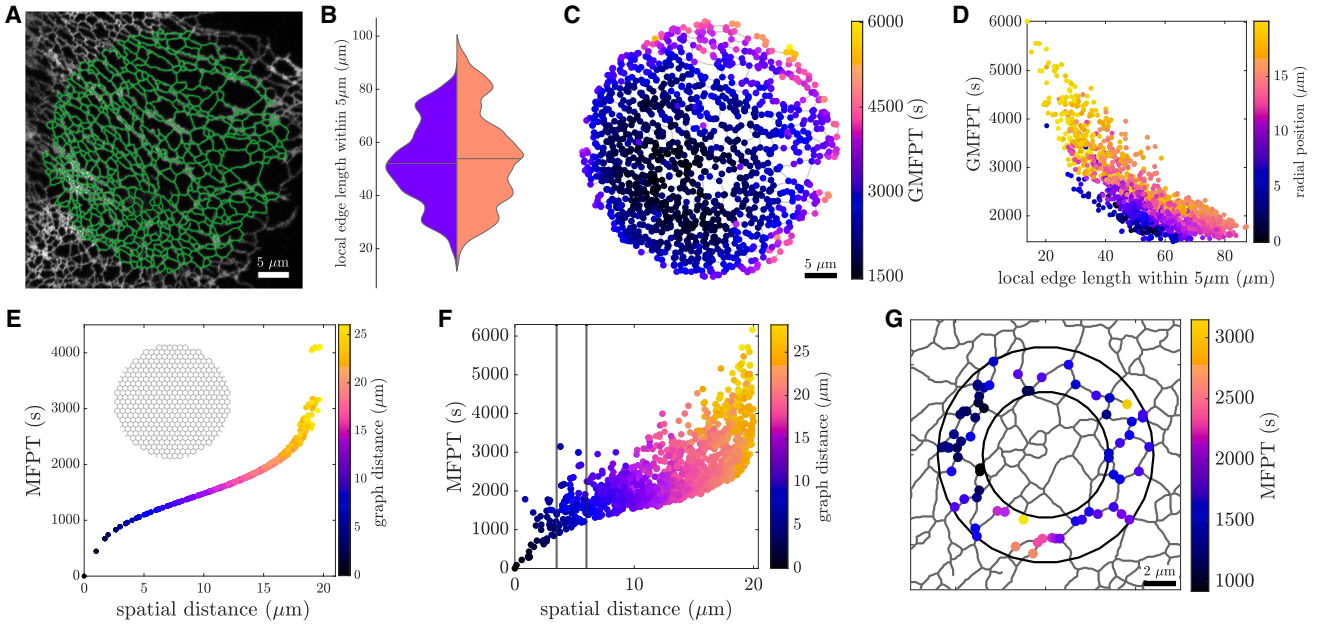

FIGURE 1 Heterogeneity in ER network structure and mean first-passage times. (*A*) Confocal image of COS7 cell expressing fluorescent ER marker (KDEL_Venus, *gray*) with extracted network structure overlay (*green*). (*B*) The distribution of local edge lengths in one cell (*left*) is similar to the corresponding distribution across multiple (n = 3) cells (*right*). (*C*) Global mean first-passage times (GMFPTs) to nodes on the example COS7 ER network shown in (*A*). (*D*) GMFPT scales inversely with local edge length; color denotes radial position from center of network. (*E*) MFPT to each network node for particles diffusing outward from the center of a circular honeycomb network. (*F*) MFPTs to all network nodes for particles diffusing outward from the center of the example ER network. Vertical lines highlight heterogeneity in a ring from 3.5 to 6 μm around the center. (*G*) MFPTs for nodes in the ring from 3.5 to 6 μm, as highlighted in (*F*). Particle diffusivity is set to $D = 1\ \mu m^2/s$ throughout. To see this figure in color, go online.

regions composed primarily of well-defined tubules and junctions. In the supporting material, we show that enlarged junctions between the tubules do not substantially affect the results (Fig. S3).

The ER density in different spatial regions can be characterized by computing the local edge length $L_{\mathrm{loc}}(x;\sigma)$, defined as the total length of network tubules that falls within distance $\sigma = 5\ \mu$m of position x. We sample local edge length for random points scattered across the domain of an example network (shown in Fig. 1 *A*). The values of $L_{\mathrm{loc}}(x;\sigma)$ span one order of magnitude, demonstrating substantial spatial heterogeneity in the ER density (Fig. 1 *B*). Notably, spatial variation in the local edge length within a single network is comparable to the variation between networks extracted from different cells.

While local edge length provides a purely structural metric of heterogeneity, we further consider the consequences of network variability on the diffusive transport of particles within the ER. One useful metric for quantifying search efficiency on spatial networks is the GMFPT (28), which gives the MFPT for a diffusing particle to reach a given node in the network, averaged over all starting nodes. This quantity can be computed analytically from the edge lengths and topology of the network (29) (see materials and methods).

The GMFPTs for different nodes in a single ER network can vary substantially (Fig. 1 *C*). Nodes near the boundary have a higher GMFPT, whereas more centrally located nodes and those in denser regions of the network exhibit the lowest GMFPTs. Some of the variation in GMFPT can be explained by the local edge length surrounding a node, as well as proximity to the boundary of the domain (Fig. 1 *D*), both a measure of centrality within the network (17). However, even nodes with similar local edge lengths and radial position can have GMFPTs that vary by a factor of 2. We note that the ER networks form a highly looped structure composed primarily of three-way junctions, with less than 5% terminal nodes. Thus, although network search times are known to vary with node degree (62), the degree of each node is insufficient to account for the observed variability of the GMFPTs. Furthermore, we consider a modified network where a randomly selected subset of node junctions is enlarged, with a target of size comparable to the tube width placed in their center. As shown in supporting material (Fig. S3), targets inside the enlarged nodes have similar search times to targets on ordinary tubule junctions. Thus, the heterogeneity in search times appears to be dictated by the edge connectivity of the network rather than by junction size.

Individual MFPTs between pairs of nodes in the network can be used to further assess heterogeneity in local transport processes. The MFPT for a particle diffusing outward from a central point to each possible target node in a uniform honeycomb network exhibits a characteristic scaling with distance, as shown in Fig. 1 *E*. Unsurprisingly, nodes that are located farther from the source tend to have higher MFPTs, with the search time increasing exponentially for the most distant population of nodes. This particular scaling of the diffusive search time relative to distance has also been observed for particles that hop actively across edges in planar network structures (63). Similar scaling is found in diffusive search for targets on the ER (Fig. 1 *F*). However, the heterogeneity of the ER network structure gives rise to a broad range of mean search times for nodes at similar distances from the source. A factor of 3 range is observed among nodes that fall within a ring from 3.5 to 6 μm from the center (Fig. 1 *F* and *G*).

Overall, we use analytic MFPTs as a measure of accessibility for different regions of the ER, either by particles starting throughout the network, or those originating from a localized source. This accessibility is shown to vary between different regions of an ER network, due to the heterogeneous density and connectivity patterns of the tubules.

Network morphology governs the nonuniform spread of photoactivated proteins

Although MFPTs are a convenient, easily computed metric of diffusive accessibility, they are difficult to probe experimentally. To directly observe the heterogeneity of diffusive spreading within the ER, we consider instead the short-time rate of arrival to nearby regions surrounding a particle source. This process is visualized by photoactivating ER membrane-associated proteins within a localized region of the network and watching their spread into surrounding regions. We note that past measurements of single-particle trajectories (24) and bulk spreading (30) of several ER membrane proteins have demonstrated that they undergo diffusive dynamics along the tubules of the peripheral ER. By contrast, aqueous proteins in the ER lumen may in some cases exhibit rapid active motion between neighboring junctions (30,64). Such active motion can substantially alter long-range transport across a network (63), and we thus do not include luminal proteins in this study.

Cultured COS7 cells are transfected with PAGFP_Calnexin, a membrane-bound ER protein with a photoactivatable fluorescent tag, as well as mCherry_KDEL as a general marker for ER structure. A single-pass photoactivating pulse is applied in a 3 μm $\times$ 3 μm square of the peripheral ER. Several frames from an example video (Video S1) are shown in Fig. 2 *A* with mCherry_KDEL in red and the PAGFP_Calnexin in green. The initial dense bolus of photoactivated proteins can be seen spreading outward through the network. We track the signal in individual small regions located equidistant from the photoactivation site. Diffusive spreading of particles over a homogeneous continuum would be expected to yield similar time courses of signal arrival to each of these regions. However, the observed PAGFP fluorescence signal over time varies substantially between the individual wedges in a single cell (Fig. 2 *B*).

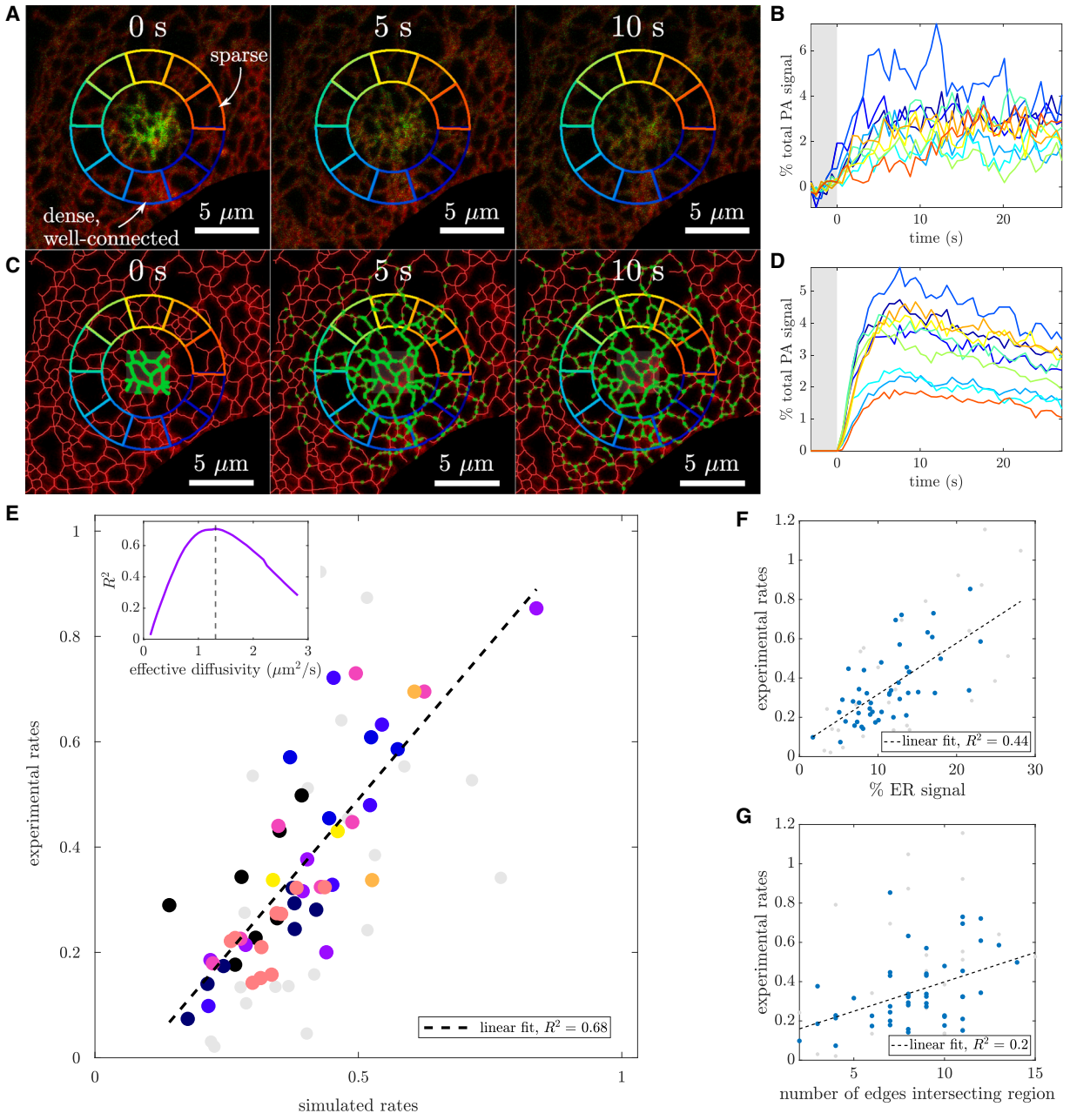

FIGURE 2 Spreading of localized bolus of particles over the ER network. (*A*) ER membrane protein PAGFP_Calnexin (*green*) is pulse-activated in a local region, whereas ER luminal marker mCherry_KDEL (*red*) serves to visualize network structure. Equidistant surrounding regions (*colored wedges*) are used to analyze signal spread. (*B*) Photoactivated signal arriving in each analyzed region, normalized by initial total signal in photoactivated zone. Gray region denotes time before photoactivation. (*C*) Snapshots of simulations on frozen ER structures extracted from first frame in *A*. (*D*) Simulated particle counts arriving in individual analysis regions, normalized by total number of particles. Gray region denotes time before photoactivation. (*E*) Correlation between signal arrival rates (slopes of signal versus time curves) for experimental and simulated data. Color indicates cell (n = 9 distinct cells). Inset: simulated protein arrival rates best match experimental arrival rates when effective diffusivity is rescaled from $D_{\text{orig}} = 1\ \mu\text{m}^2/\text{s}$ to $D_{\text{eff}} = 1.3\ \mu\text{m}^2/\text{s}$ (*dashed line*). (*F*) Correlation of experimental signal arrival rate in individual regions versus the fraction of ER marker signal in that region. (*G*) Correlation of experimental signal arrival rate with the number of edges intersecting the boundary of each region. Regions removed due to filtering are shown in gray in (*E*)–(*G*). To see this figure in color, go online.

This variability can be attributed to the heterogeneous distribution and connectivity of the ER tubules. Intuitively, the blue region contains dense, highly connected tubules and has the strongest and fastest-growing photoactivation signal. By contrast, the orange region is poorly connected to the activation site and exhibits the smallest initial signal growth.

To account for the observed differences in signal arrival rates due to ER morphology, we extracted the ER network

structure in the vicinity of the photoactivation site and carried out agent-based simulations of diffusing particles initiated at the site (Fig. 2 *C*, Video S2). Quantifying the number of simulated particles accumulating in each region over time allows for a direct comparison between simulated and observed fluorescent signal. For both the experimental and simulated data, we normalize the measured signal in each region by the initial total signal within a disk of 3.5 μm radius centered on the photoactivation zone (inner circle in Fig. 2 *A* and *C*). Thus, the reported signal traces are given in terms of the fraction of initially photoactivated particles present in a given region at a given time. The normalized simulated signal (Fig. 2 *D*) exhibits similar behavior to the experimental results, with well-connected dense regions receiving more signal faster than poorly connected and sparse ER regions.

To partially incorporate the effect of ER network rearrangement over time, the photoactivation simulations are run on network structures extracted for every frame of the experimental movie (at time interval 0.6 s). The signal over time is then averaged across the ensemble of simulations on all of these different network structures. This ensemble-averaged simulated signal is used in the subsequent analysis. Analogous results using only a single network structure can be found in the supporting material.

To quantitatively compare protein arrival rates in the experimental and simulated ER networks, we extract the slope of the normalized signal curves up to 10 s after photoactivation. These slopes (referred to as "arrival rates") serve as a simple metric that provides information about the spatial heterogeneity of protein spreading around the photoactivation site. Because our simulations are carried out on network structures extracted from the experimental images, it is possible to directly compare the rate of signal arrival in matched regions between experimental and simulated data (Fig. 2 *E*). Regions where the extracted network length was a poor match for the observed ER marker (mCherry_KDEL) fluorescence, or where the ER marker showed large fluctuations over time, were filtered out of the analysis (gray dots; see materials and methods for details). Notably, the variability of measured rates between regions within each individual cell (same color dots) is comparable to the intercell variability (different color dots), indicating that the arrival rates are similarly heterogeneous in all the observed cells. The experimental and simulated arrival rates show a direct correlation: $R^2 = 0.68$, obtained from a linear fit. The high correlation implies that diffusive particle motion over an ER network is a good predictor of signal arrival to different regions.

Notably, the simulation time can be rescaled to effectively represent particles of different diffusivity (see materials and methods for details). We compare the correlation of signal arrival rates between experimental measurements and simulations with different time scaling. The simulations that best correlate with experimental values correspond to a particle diffusivity of $D_{\text{eff}} \approx 1.3\ \mu\text{m}^2/\text{s}$ (Fig. 2 *E*, inset), a value that is similar in magnitude to previous measurements of diffusivity via single-particle tracking for other ER membrane proteins (24). This result demonstrates that particle diffusivity in the ER can be measured by quantifying signal arrival rates to different structural regions of network, all located relatively close to the photoactivated zone, without the need for tracking longer-range spread across the cell (30).

In order to test whether particle diffusion simulations are more predictive than simpler metrics of network structure, we also compare the experimental arrival rates to the mCherry_KDEL ER signal in each region. A linear fit (Fig. 2 *F*) demonstrates there is some correlation between the two ($R^2 = 0.44$), but variation in the ER volume within each region (as measured by mCherry_KDEL signal) cannot capture the full variability in protein spreading rates. A simple metric for local connectivity, the number of edges crossing the boundary of each wedge region, is shown to be roughly correlated (Fig. 2 *G*, $R^2 = 0.2$), but it also does not provide a strong predictor of protein arrival rates. Thus, the distribution of protein spreading rates in live cells is best modeled by simulations that take into account not just the local ER density in a region but also the connectivity of the surrounding network together with the dynamics of diffusive particles moving through this network.

Slow ER network dynamics have little effect on particle spreading

The ER network in a living cell is itself a dynamic structure, with network rearrangements occurring over tens-of-second timescales as a result of attachment to motile organelles, molecular motors, and growing microtubule tips (32,57,65). In comparing the measured rates of protein spread to simulations of diffusing particles (Fig. 2 *E*), we account for time variation in ER architecture by averaging over network structures extracted from each frame.

To gain a better sense of how ER tubule dynamics may contribute to the spread of photoactivated proteins, we incorporate network rearrangements directly into our simulations, by treating the ER as a "minimal network" with tubules subject to growth and constant tension (43). These synthetic dynamic networks (described in the materials and methods) mimic the rearrangements of the ER over time, including new tubule growth, junction sliding, and the merging of junctions.

The two parameters primarily responsible for determining the equilibrium properties are node mobility (units of μm/s, sets speed with which nodes rearrange) and new tubule growth rate (units of $\mu\text{m}^{-1}\text{s}^{-1}$, rate at which new tubules are pulled out of existing tubules). Other parameters, such as node diffusivity and new tubule growth speed, play a secondary role in the parameter regimes considered here. Input parameters to the model are set so that network

properties at equilibrium match the ER network in COS7 cells. Specifically, the modeled networks match the measured rate of new tubule formation (Video S3) and the steady-state average edge length in the network. For comparison, we also ran simulations of networks that exhibit faster dynamics, with both tubule growth rate and node mobility increased by a factor of 2. These faster networks have the same steady-state network structure but rearrange twice as rapidly.

For each of these dynamic networks, 16 separate photoactivation events are simulated in different regions of the network. Particles are initiated within 3 μm $\times$ 3 μm patches and allowed to diffuse through the structure either on a static network or concurrently with the network dynamics (Fig. 3 *A*, Video S4). We compare the rate of particles arriving to equidistant regions surrounding the initiation zone both with and without network dynamics.

When the particle simulations are run on a single static network structure, the arrival rates are moderately well correlated ($R^2 = 0.87$) with the rates observed for simulations on dynamic networks (Fig. 3 *B*). Faster dynamics in the synthetic networks reduces this correlation to $R^2 = 0.78$. Intuitively, as the rearrangements occur more quickly, diffusive particles encounter more extensive changes in structure during the 10-s timescale of the measurement.

Notably, even when network dynamics are twice as rapid as the experimentally observed dynamics of the ER network, the static network approximation is a good predictor for particle arrival rates. We can estimate the importance of active network rearrangements versus the diffusive motion of the particles by considering an effective Péclet number for the system. The mobility parameter for the dynamic networks ($b = 0.05\ \mu$m/s) sets a typical velocity for tension-driven sliding. Over a length scale of 10 μm (the size of the analyzed region), the corresponding Péclet number for a protein within the network is $\mathrm{Pe} = vL/D \approx 0.5$. Doubling the rate of ER rearrangement doubles this Péclet number. Because this dimensionless quantity is close to or below $\mathrm{Pe} = 1$, the motion of the particles is dominated by their diffusivity rather than by the tubule rearrangement dynamics.

The moderate effect of network dynamics on particle spreading can be partly accounted for by running simulations on many individual static network structures extracted at different points in time. We perform this analysis using snapshots of our simulated dynamic networks and averaging the signal in each region at each time point. For this ensemble-averaged data, the arrival rates on static and dynamic networks become more closely correlated (Fig. 3 *C*), even in the case of rapid network rearrangements ($R^2 = 0.91$). Thus, the effect of network dynamics is almost entirely accounted for by averaging multiple static simulations on consecutive network structures. These results on synthetic dynamic networks validate the use of the same ensemble averaging approach when analyzing experimental data.

ER structure directs reaction locations

The ER does more than simply serve as a transport hub for proteins, lipids, and ions; it also plays a role in protein synthesis and quality control (35,42), as well as forming functionally important contact sites with other organelles (33). The formation of reactive complexes, exit sites for protein

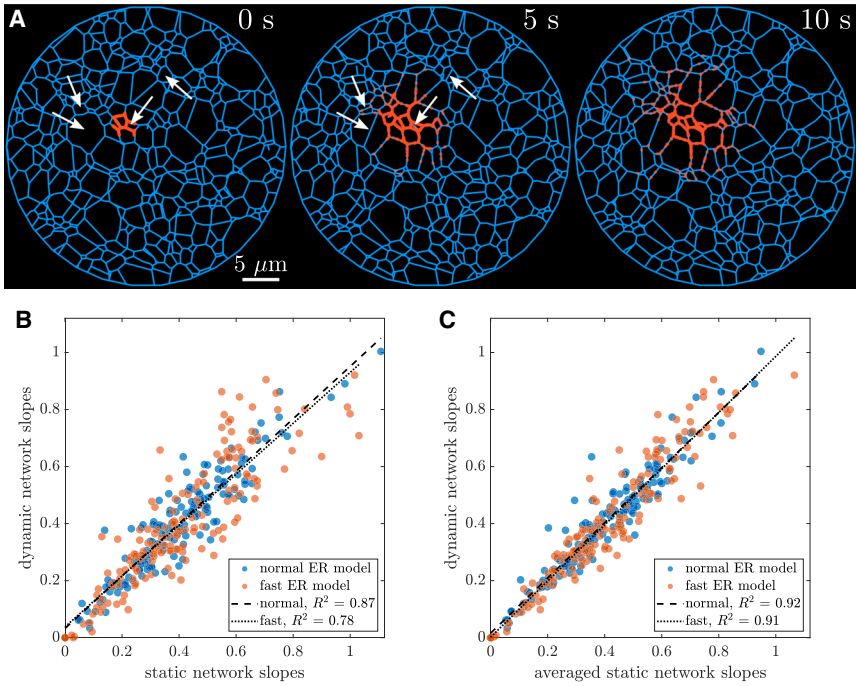

FIGURE 3 ER network dynamics does not substantially affect particle spreading. (*A*) Snapshots from simulation of diffusing particles spreading from a local region, on a minimal network dynamic model. Network edges are blue, and a subset (500) of the simulated particles ($D = 1\ \mu$m^2/s) are shown in orange. White arrows highlight several new edges that grew between the first and second snapshots. (*B*) Correlation of signal arrival rate (slope of signal-versus-time curves) to individual regions, comparing simulations on a single static network structure and on dynamic minimal network model with turnover timescales comparable to ER dynamics (*blue*) or 2$\times$ faster (*red*). (*C*) Comparison of signal arrival rates for simulation on a dynamic network versus simulations of particles diffusing on a static network, averaged over static structures from individual snapshots of the minimal network. The average static rates are obtained in the same manner as in the analysis of experimental data. To see this figure in color, go online.

export, and contact site assemblies requires multiple intra-ER particles to find each other within the network. In order to better understand how diffusion-mediated biochemical reactions are impacted by ER morphology, we simulate reactive particle pairs diffusing on extracted ER network structures (Fig. 4 *A*). From these simulations, both the spatial locations of reactions on the network as well as the distribution of reaction times are extracted.

Many previous studies of diffusive processes on networks have focused on the temporal properties of reactions or exit times (e.g., MFPTs, extreme statistics, and full FPT distributions (16,26,29)), without considering in detail where those reactions occur. Here, we provide fresh insight by analyzing the spatial locations, as well as temporal distributions, of pairwise reactions on the ER. Pairs of particles are distributed randomly across the network to begin the simulation. Each pair diffuses along the edges of the network until the two particles come into contact with one another. At this point, they react, and the position and time of reaction is recorded. The network edges are meshed into segments of length $l \approx 0.2\ \mu$m, and the normalized reaction density in mesh cell i is defined as

$$\gamma_i = \frac{\#\text{ of reactions in cell } i}{\#\text{ of particle pairs}} \times \frac{\text{total network length}}{l}. \quad (5)$$

When averaged over an entire network, $\langle\gamma\rangle = 1$. Simulations on the ER network structure demonstrate that paired particle reaction locations are heterogeneous (Fig. 4 *B*, middle panel), with some regions showing a particularly high reaction density γ. Certain tubule segments are more likely to serve as the reaction site, due to their enhanced connectivity to the rest of the network. The normalized reaction density correlates with the inverse of the GMFPT (Fig. 4 *C*), indicating that these highly reactive regions are in fact easier to find by diffusing particles.

These simulations imply that heterogeneity in ER structure and accessibility is expected to result in diffusive particle reactions becoming concentrated within certain regions. For comparison, we repeat the simulations on two synthetic network structures: a homogeneous honeycomb network (Fig. 4 *B*,

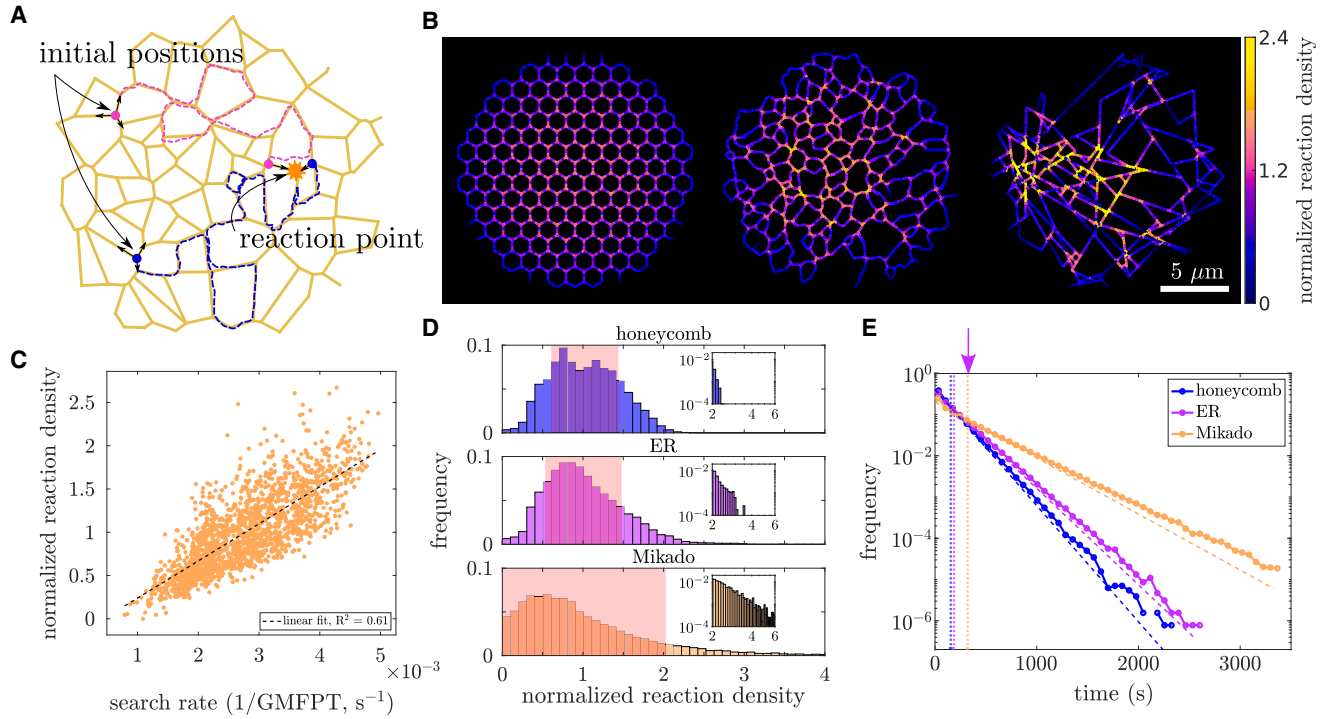

FIGURE 4 ER heterogeneity leads to hot spots of paired particle encounters. (*A*) Schematic of paired particle simulations. Pairs of particles (*pink and blue circles*) diffuse through the network (*dashed lines indicate trajectories*) until they encounter and react. (*B*) Normalized reaction density on three example networks, each with similar total edge length and spatial size. For each discretized segment of network, the fraction of simulated reactions occurring within that segment is normalized by the fraction of total edge length contained within that segment. Left panel, a homogeneous honeycomb network with the same average edge length as the ER network in the middle panel. Middle panel, ER network is extracted from a section of COS7 peripheral ER; it exhibits regions of higher reaction density than the homogeneous honeycomb (*bright yellow segments*). In the right panel, the normalized reaction density on a highly heterogeneous synthetic, Mikado-like network, exhibiting even more pronounced hot spots than the ER. (*C*) Paired reaction density on each segment of the ER is roughly correlated with the inverse of the global mean first-passage time (GMFPT) to that segment. (*D*) Distribution of reaction densities for all discretized segments in honeycomb, ER, and Mikado-like networks, showing increasing heterogeneity in the densities. Insets show long tail of distribution plotted on log-log axes. Mean for each distribution is 1, and red overlay denotes standard deviation. (*E*) Distributions of paired reaction times in the three network structures. Dotted lines mark the mean reaction time. Dashed lines show exponential decay for a Poisson process with the same mean. The target-averaged GMFPT on the ER networks indicated by the purple arrow is more than twice the mean pair reaction time. Results in (*C–E*) were computed for eight distinct circular regions of the ER (17 μm diameter), extracted from three different cells.To see this figure in color, go online.

left panel) and a highly heterogeneous modified Mikado network (58) (Fig. 4 *B*, right panel; see materials and methods for details). Both of these networks have the same spatial extent and total network length as the extracted ER networks. This allows for a quantitative comparison of the reaction density and reaction time distributions between all three families of networks.

As expected, reaction locations are more uniformly distributed on the honeycomb network. Within this homogeneous network, reactions are slightly more likely to occur at junction nodes rather than along the edges, in keeping with past work showing random walkers are more likely to encounter each other at higher-degree network nodes (62). There is also a dearth of reactions at the network boundary, mirroring the increased GMFPT in the boundary region (Fig. 1 *C*). The ER networks show a similar drop-off in reaction density along edges compared with junctions, as well as at the boundary. Moreover, due to the heterogeneous network density and connectivity, reactions are more concentrated into certain junctions within the network, with a higher maximum reaction density at these select junctions than is observed in the more uniform honeycomb. Reactions are further concentrated in the modified Mikado networks, demonstrating that more heterogeneous networks exhibit a broader range of reaction densities. This effect is quantified in Fig. 4 *D*, where a longer tail is visible in the distribution of normalized reaction densities for ER and Mikado networks, compared with the honeycomb. The morphology and connectivity of a network can thus tune the spatial distribution of reaction locations.

Network structure is not only responsible for shaping the spatial profile of reaction density, but can also affect the overall reaction time (26,28). The distribution of pairwise reaction times on each network exhibits exponential scaling (Fig. 4 *E*), as for a Poisson process with a single dominant timescale. As noted in previous work, the mean reaction time on the ER (dashed purple line) is less than half of the target-averaged GMFPT (purple arrow) (29). Even though there are higher spatial reaction densities in the more heterogeneous networks, mean reaction time is lowest in the homogeneous honeycombs and highest in the modified Mikado networks (Fig. 4 *E*). Thus, there is a trade-off between locally concentrating reactions in space versus minimizing overall reaction time.

Proximity to well-connected perinuclear ER enhances accessibility

In addition to variations in local connectivity, a further source of heterogeneity for the peripheral ER network arises from the presence of extended sheet-like structures in the perinuclear zone (Fig. 5 *A*). Although the morphology of

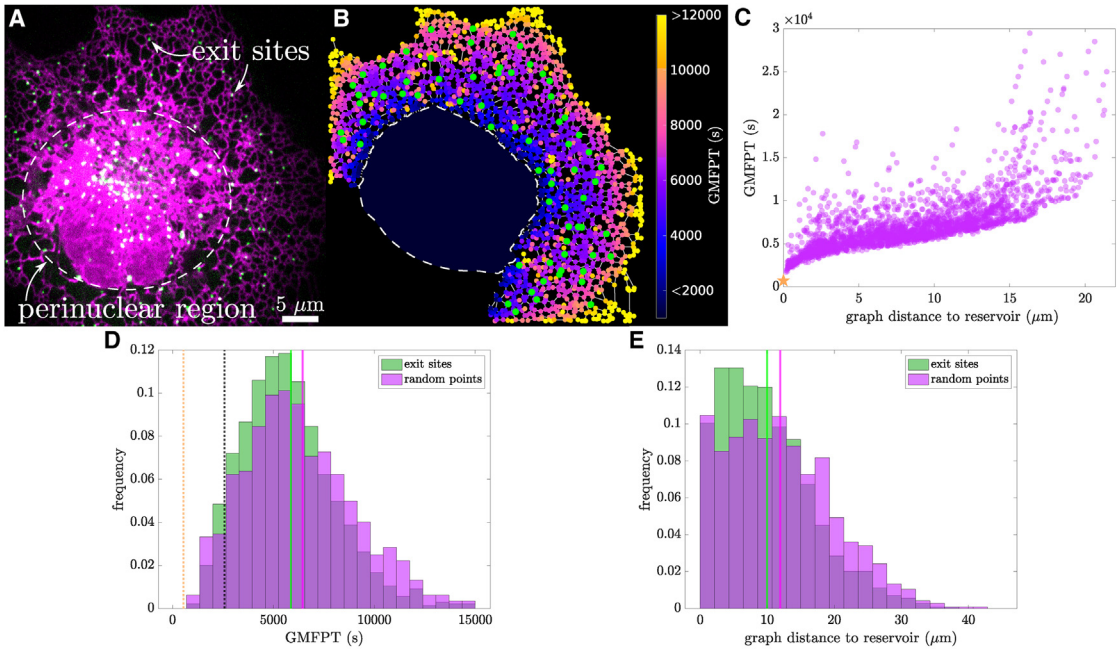

FIGURE 5 Concentration of ERES in regions of the peripheral ER with high search rate. (*A*) Image of the ER (*magenta*, mCherry_KDEL) and ERES (*green*, GFP_Sec24d) of a COS7 cell. (*B*) Extracted network structure of peripheral ER (excluding nucleus and perinuclear sheet regions). Junctions are colored by their effective search time (GMFPT, units of s). ERES positions are shown in green. Dashed line indicates excised nucleus and perinuclear sheet region, with interior color corresponding to GMFPT to a target at the center. (*C*) The GMFPT scales with graph distance to the perinuclear reservoir, for the example network shown in (B). Orange star indicates GMFPT to target in reservoir. (*D*) ERES positions exhibit lower search times than random points on the network. Distributions include 1443 exit sites and the same number of random points extracted from the peripheral ER of 22 different COS7 cells. Green and magenta vertical lines indicate mean of each distribution; orange dotted line indicates the mean GMFPT (averaged over all networks) to a target in the reservoir center; black dotted line gives mean GMFPT to full population of peripheral and perinuclear ERES targets. (*E*) Distributions of graph distance to the reservoir for 1443 exit sites and 1443 random points extracted from the peripheral ER of 22 different COS7 cells. To see this figure in color, go online.

the perinuclear region cannot be well resolved with confocal microscopy, electron microscopy studies have shown that the ER near the cell nucleus consists of stacks of sheet-like structures, connected with spiral ramps (2). We consider how the presence of a large perinuclear ER reservoir may affect search times for targets in the peripheral network. For simplicity, we do not directly model the structure of the perinuclear ER, but we rather treat it as a large, flat, disk-like region connected along its boundary to the peripheral network. This approximation neglects transport between the stacked ER sheets themselves, which has previously been shown to be accelerated by spiral connecting ramps (9).

We expand our model to treat the perinuclear reservoir as an extremely large node, connected to many network tubules. We then compute the GMFPT to each peripheral node, assuming that particles can start anywhere in the peripheral network or the perinuclear region, in proportion to the available surface area. Within the perinuclear zone, particles effectively move through two-dimensional diffusion, returning to the peripheral network through narrow exits into individual tubules, as described in supporting material, Section S2. Due to the large area of the perinuclear zone, most particles enter this region before finding any given target on the peripheral network. As a result, targets located near the perinuclear region have lower GMFPTs. This effect leads to a gradient of accessibility for the peripheral ER as a function of distance from the perinuclear zone (Fig. 5 *B* and *C*). A target placed in the center of the perinuclear zone has a search time comparable with the lowest values for the peripheral network.

Given the variation in search times for different regions of the peripheral ER, we next sought to examine whether certain ER-associated protein assemblies may be more likely to localize to more accessible regions. Specifically, we explore the distribution of ERES, which serve as the export hubs for newly synthesized proteins in the ER (39, 40). The mechanism underlying the distribution of exit sites on the network is not well understood, although prior work has suggested they may arise from a process of confined diffusive aggregation (66). The ERES are found both on the perinuclear and the peripheral ER (Fig. 5 *A*). Because puncta in the well-mixed perinuclear region are expected to all have similar accessibilities, we focus here on those ERES located in the peripheral network.

We extract ERES puncta locations using several different markers for the exit sites (Fig. 5 *A*, details in materials and methods) and project the peripheral ERES locations onto the extracted ER network structure (Fig. 5 *B*). We next calculate the GMFPT to each peripheral ERES position and compare the distribution of these times to that expected for randomly selected locations along the networks (Fig. 5 *D*). The distribution of search times at the exit sites (mean $\pm$ std: $5.9 \pm 2.8 \times 10^3$ s) is shifted to smaller values compared with the randomized control (mean $\pm$ std: $6.5 \pm 3.1 \times 10^3$ s). Although the magnitude of the shift is modest, this difference is statistically significant ($p \ll 10^{-6}$ by a one-sided Student's *t*-test) due to the large number of ERES puncta sampled. The ERES are thus disproportionately likely to be found in more accessible regions of the peripheral network. The lower search times to peripheral ERES locations can be explained by their tendency to be located near the perinuclear zone and their depletion from the distal regions of the periphery (Fig. 5 *E*). Exit sites located in the perinuclear zone itself (approximated as targets in the center of the reservoir) are expected to have the lowest search times (Fig. 5 *D*, dotted orange line). Because a substantial fraction of ERES are found in the perinuclear zone, the overall average search time to the exit sites (black dotted line) is approximately twofold lower than the search time to randomly selected peripheral targets. Overall, localization of ERES within and nearby the perinuclear region is expected to enhance their accessibility for diffusively searching particles.

These results indicate a potential structure-function relationship for the peripheral ER network. Structural heterogeneity in the network, both in terms of connectivity and in terms of proximity to the perinuclear ER, translates to heterogeneous search times for diffusing particles. In turn, certain multiprotein assemblies within the ER network appear to be localized to the more accessible regions, where they can be more easily reached by other diffusive particles.

CONCLUSION

In this work, we highlight the heterogeneous connectivity of the tubular ER network and its consequences for diffusive particle transport. We extract peripheral ER network structures from live-cell confocal images of COS7 cells and analytically compute MFPTs for particles diffusing over these networks. These calculations allow us to quantify the variability in diffusive accessibility within individual ER architectures. The GMFPT to individual nodes within the network is found to vary by up to fourfold due to the heterogeneous connectivity of the network.

We then directly visualize the local spreading of ER membrane proteins from an initial region of pulsed photoactivation. Signal arrival rates to distinct regions equidistant from the photoactivated center show marked disparities (varying by more than a factor of 4 within a single cell). We compare these measurements to simulations of diffusing particles on the visualized ER network structure and show that the simulated rates of arrival to distinct regions show strong agreement with experimental data. These results demonstrate the importance of network structure in guiding the observed heterogeneity in protein spread.

By modifying and extending a model for "minimal networks" driven by membrane tension and new tubule growth (43), we assess the effect of ER network rearrangements on

protein spread. The substantial separation of timescales between network dynamics and protein diffusivity leads to only a marginal predicted effect of tubule rearrangement on the motion of proteins within the ER.

Additionally, we simulate pairs of reactive particles diffusing through the ER and demonstrate that the structural heterogeneity of the network gives rise to effective hot spots where encounters are more likely to occur. The proximity of targets to the well-connected perinuclear zone provides another source of variable accessibility with the network. Notably, an analysis of ERES positions across the peripheral ER indicates that the location of these structures is biased toward the more accessible regions near the perinuclear zone and away from the less accessible distal periphery of the cell.

We note that the ER models in this study are intentionally highly simplified, reducing the complex membrane-enclosed geometry of the ER to a network of effectively one-dimensional tubules. These simplifications make it possible to focus on the role of cellular-scale network connectivity and rearrangements in particle transport. The simple structural model is sufficient to reproduce the observed heterogeneous protein arrival rates to different network regions in photoactivation experiments. More detailed structural models could include variability in tubule diameter (67,68) as well as scattered peripheral sheets (69), which may themselves be perforated with holes (61) or composed of dense tubular matrices (4). Exploring the effect of these structures on particle transport forms a potentially interesting avenue for future work.

The network dynamics model employed here aims to isolate the key important features governing ER rearrangements—namely, the formation of new tubules and the tension-driven movement of junctions (32,43,70). Although network dynamics are shown to have little impact on protein diffusion, they are expected to play a greater role in the motion of larger and slower-moving ER-associated bodies such as the ERES (71). Furthermore, it is possible that directed flows of luminal and/or membrane contents may be associated with the growth and shrinking of ER tubules, as implied by recent evidence that new tubule growth is followed by a delayed widening and infilling with Climp63 spacer proteins (68). Although the spatial extent and magnitude of such flows is not currently established, they could more extensively contribute to modulating intra-ER protein motion.

The transport, quality control, and export of proteins in the ER are essential biological processes in the early secretory pathway. These processes require a variety of encounters between newly manufactured proteins, chaperones, and regulatory factors. The structural heterogeneity of the ER network implies that certain regions may allow for more efficient encounters between binding partners. Notably, however, the effect of morphology becomes important only in the regime of diffusion-limited kinetics when the particles are sparsely scattered over the network (26). The sequestration of some quality control machinery to specific regions of the ER (42) implies that long-range diffusive search by proteins through the network may be an important factor in the kinetics of such pathways.

In addition to protein transport, the results described here apply to any diffusive particles contained in the membrane or lumen of the peripheral ER network. This includes ions such as calcium, as well as the buffer proteins that bind to them. In particular, we would expect the demonstrated structural heterogeneity of the ER to lead to more rapid calcium release in better-connected regions of the network. Given that calcium homeostasis and signaling is one of the key functional roles of the ER, heterogeneous transport could thus provide an important link between physical structure and biological function. Furthermore, it would be interesting to explore whether contacts between the peripheral ER and other cellular structures, such as mitochondria, tend to preferentially occur at highly connected regions, which may facilitate the delivery of lipids or ions across these contacts (72–74).

Through the use of experiments paired with quantitative image analysis and computational modeling, our results demonstrate how morphology guides particle transport and reactions in the ER, with broad implications for diffusive transport in any intracellular network structure.

SUPPORTING MATERIAL

Supporting material can be found online at https://doi.org/10.1016/j.bpj.2023.06.022.

AUTHOR CONTRIBUTIONS

Z.C.S., L.M.W., and E.F.K. conceived and designed the research and wrote the manuscript. Z.C.S. and E.F.K. developed and implemented the model for both particle diffusion and network dynamics. Z.C.S. analyzed imaging and simulation data. K.K., M.V., L.C., and L.M.W. generated experimental data and performed imaging studies.

ACKNOWLEDGMENTS

We thank Dr. Edward Avezov and Dr. Eric Arnoys for helpful discussions and the Van Andel Institute Optical Imaging Core (RRID: SCR_021968), especially Corinne Esquibel, for their assistance with the Zeiss LSM 880. Funding was provided by the National Science Foundation (Grant ID #2034482 to E.F.K. and #2034486 to L.M.W.), a Cottrell Scholar Award from the Research Corporation for Science Advancement to E.F.K., and a UCSD Chancellor Funded Research Grant. Sponsored also in part from the Supporting Structures: Innovative Partnerships to Enhance Bench Science at CCCU Member Institutions program (SCIO, John Templeton Foundation, and the MJ Murdock Charitable Trust).

DECLARATION OF INTERESTS

The authors declare no competing interests.

REFERENCES

1. Dieteren, C. E. J., S. C. A. M. Gielen, …, W. J. H. Koopman. 2011. Solute diffusion is hindered in the mitochondrial matrix. *Proc. Natl. Acad. Sci. USA.* 108:8657–8662.
2. Terasaki, M., T. Shemesh, …, M. M. Kozlov. 2013. Stacked endoplasmic reticulum sheets are connected by helicoidal membrane motifs. *Cell.* 154:285–296.
3. Wang, S., H. Tukachinsky, …, T. A. Rapoport. 2016. Cooperation of the ER-shaping proteins atlastin, lunapark, and reticulons to generate a tubular membrane network. *Elife.* 5, e18605.
4. Nixon-Abell, J., C. J. Obara, …, J. Lippincott-Schwartz. 2016. Increased spatiotemporal resolution reveals highly dynamic dense tubular matrices in the peripheral ER. *Science.* 354:aaf3928.
5. Burute, M., and L. C. Kapitein. 2019. Cellular logistics: unraveling the interplay between microtubule organization and intracellular transport. *Annu. Rev. Cell. Dev. Biol.* 35:29–54.
6. Ross, J. L., M. Y. Ali, and D. M. Warshaw. 2008. Cargo transport: molecular motors navigate a complex cytoskeleton. *Curr. Opin. Cell Biol.* 20:41–47.
7. S Mogre, S., A. I. Brown, and E. F. Koslover. 2020. Getting around the cell: physical transport in the intracellular world. *Phys. Biol.* 17, 061003.
8. Agrawal, A., Z. C. Scott, and E. F. Koslover. 2022. Morphology and transport in eukaryotic cells. *Ann. Rev. Biophys.* 51:247–266.
9. Huber, G., and M. Wilkinson. 2019. Terasaki spiral ramps and intracellular diffusion. *Phys. Biol.* 16, 065002.
10. Bénichou, O., C. Chevalier, …, R. Voituriez. 2010. Geometry-controlled kinetics. *Nat. Chem.* 2:472–477.
11. Takahashi, K., S. Tănase-Nicola, and P. R. Ten Wolde. 2010. Spatio-temporal correlations can drastically change the response of a MAPK pathway. *Proc. Natl. Acad. Sci. USA.* 107:2473–2478.
12. Abel, S. M., J. P. Roose, …, A. K. Chakraborty. 2012. The membrane environment can promote or suppress bistability in cell signaling networks. *J. Phys. Chem. B.* 116:3630–3640.
13. Galstyan, V., K. Husain, …, R. Phillips. 2020. Proofreading through spatial gradients. *Elife.* 9, e60415.
14. Chubynsky, M. V., and G. W. Slater. 2014. Diffusing diffusivity: a model for anomalous, yet Brownian, diffusion. *Phys. Rev. Lett.* 113, 098302.
15. Jain, R., and K. L. Sebastian. 2016. Diffusing diffusivity: survival in a crowded rearranging and bounded domain. *J. Phys. Chem. B.* 120:9215–9222.
16. Lanoiselée, Y., N. Moutal, and D. S. Grebenkov. 2018. Diffusion-limited reactions in dynamic heterogeneous media. *Nat. Commun.* 9:1–16.
17. Barthélemy, M. 2011. Spatial networks. *Phys. Rep.* 499:1–101.
18. Bryant, S. L., D. W. Mellor, and C. A. Cade. 1993. Physically representative network models of transport in porous media. *AIChE J.* 39:387–396.
19. Williams, A. H., C. O'Donnell, …, T. O'Leary. 2016. Dendritic trafficking faces physiologically critical speed-precision tradeoffs. *Elife.* 5, e20556.
20. Sartori, F., A.-S. Hafner, …, T. Tchumatchenko. 2020. Statistical Laws of Protein Motion in Neuronal Dendritic Trees. *Cell Rep.* 33, 108391.
21. Lizana, L., and Z. Konkoli. 2005. Diffusive transport in networks built of containers and tubes. *Phys. Rev. E.* 72, 026305.
22. Li, R., J. A. Fowler, and B. A. Todd. 2014. Calculated rates of diffusion-limited reactions in a three-dimensional network of connected compartments: application to porous catalysts and biological systems. *Phys. Rev. Lett.* 113, 028303.
23. Lin, C., R. R. White, …, P. Ashwin. 2017. Modeling endoplasmic reticulum network maintenance in a plant cell. *Biophys. J.* 113:214–222.
24. Sun, Y., Z. Yu, …, E. F. Koslover. 2022. Unraveling trajectories of diffusive particles on networks. *Phys. Rev. Res.* 4, 023182.
25. Tikhomirova, M. S., A. Kadosh, …, R. W. Klemm. 2022. A role for endoplasmic reticulum dynamics in the cellular distribution of microtubules. *Proc. Natl. Acad. Sci. USA.* 119, e2104309119.
26. Viana, M. P., A. I. Brown, …, S. M. Rafelski. 2020. Mitochondrial fission and fusion dynamics generate efficient, robust, and evenly distributed network topologies in budding yeast cells. *Cell. Syst.* 10:287–297.e5.
27. Zamponi, N., E. Zamponi, …, D. R. Chialvo. 2018. Mitochondrial network complexity emerges from fission/fusion dynamics. *Sci. Rep.* 8:363.
28. Brown, A. I., L. M. Westrate, and E. F. Koslover. 2020. Impact of global structure on diffusive exploration of organelle networks. *Sci. Rep.* 10:4984.
29. Scott, Z. C., A. I. Brown, …, E. F. Koslover. 2021. Diffusive search and trajectories on tubular networks: a propagator approach. *Eur. Phys. J. E.* 44:80.
30. Konno, T., P. Parutto, …, A. Agrawal. 2021. Endoplasmic Reticulum morphological regulation by RTN4/NOGO modulates neuronal regeneration by curbing luminal transport. Preprint at bioRxiv. https://doi.org/10.1101/2021.05.10.441946.
31. Yang, Z., and E. F. Koslover. 2023. Diffusive exit rates through pores in membrane-enclosed structures. *Phys. Biol.* 20:026001. https://doi.org/10.1088/1478-3975/acb1ea.
32. Westrate, L. M., J. E. Lee, …, G. K. Voeltz. 2015. Form follows function: the importance of endoplasmic reticulum shape. *Annu. Rev. Biochem.* 84:791–811.
33. Wu, H., P. Carvalho, and G. K. Voeltz. 2018. Here, there, and everywhere: The importance of ER membrane contact sites. *Science.* 361, eaan5835.
34. Balla, T., Y. J. Kim, …, J. Pemberton. 2019. Lipid dynamics at contact sites between the endoplasmic reticulum and other organelles. *Annu. Rev. Cell. Dev. Biol.* 35:85–109.
35. Ellgaard, L., and A. Helenius. 2003. Quality control in the endoplasmic reticulum. *Nat. Rev. Mol. Cell Biol.* 4:181–191.
36. Phillips, B. P., N. Gomez-Navarro, and E. A. Miller. 2020. Protein quality control in the endoplasmic reticulum. *Curr. Opin. Cell Biol.* 65:96–102.
37. Barlowe, C., L. Orci, …, R. Schekman. 1994. COPII: a membrane coat formed by Sec proteins that drive vesicle budding from the endoplasmic reticulum. *Cell.* 77:895–907.
38. Matsuoka, K., L. Orci, …, T. Yeung. 1998. COPII-coated vesicle formation reconstituted with purified coat proteins and chemically defined liposomes. *Cell.* 93:263–275.
39. Watson, P., A. K. Townley, …, D. J. Stephens. 2006. Sec16 defines endoplasmic reticulum exit sites and is required for secretory cargo export in mammalian cells. *Traffic.* 7:1678–1687.
40. Westrate, L. M., M. J. Hoyer, …, G. K. Voeltz. 2020. Vesicular and uncoated Rab1-dependent cargo carriers facilitate ER to Golgi transport. *J. Cell Sci.* 133:jcs239814.
41. Kamhi-Nesher, S., M. Shenkman, …, G. Z. Lederkremer. 2001. A novel quality control compartment derived from the endoplasmic reticulum. *Mol. Biol. Cell.* 12:1711–1723.
42. Sontag, E. M., W. I. M. Vonk, and J. Frydman. 2014. Sorting out the trash: the spatial nature of eukaryotic protein quality control. *Curr. Opin. Cell Biol.* 26:139–146.
43. Lin, C., Y. Zhang, …, P. Ashwin. 2014. Structure and dynamics of ER: minimal networks and biophysical constraints. *Biophys. J.* 107:763–772.
44. English, A. R., and G. K. Voeltz. 2013. Rab10 GTPase regulates ER dynamics and morphology. *Nat. Cell Biol.* 15:169–178.
45. Friedman, J. R., L. L. Lackner, …, G. K. Voeltz. 2011. ER tubules mark sites of mitochondrial division. *Science.* 334:358–362.
46. Zurek, N., L. Sparks, and G. Voeltz. 2011. Reticulon short hairpin transmembrane domains are used to shape ER tubules. *Traffic.* 12:28–41.

47. Bhattacharyya, D., and B. S. Glick. 2007. Two mammalian Sec16 homologues have nonredundant functions in endoplasmic reticulum (ER) export and transitional ER organization. *Mol. Biol. Cell.* 18:839–849.

48. Stephens, D. J., N. Lin-Marq, …, J.-P. Paccaud. 2000. COPI-coated ER-to-Golgi transport complexes segregate from COPII in close proximity to ER exit sites. *J. Cell Sci.* 113:2177–2185.

49. Richards, C. I., R. Srinivasan, …, H. A. Lester. 2011. Trafficking of α4* nicotinic receptors revealed by superecliptic phluorin: effects of a β4 amyotrophic lateral sclerosis-associated mutation and chronic exposure to nicotine. *J. Biol. Chem.* 286:31241–31249.

50. Patterson, G. H., and J. Lippincott-Schwartz. 2002. A photoactivatable GFP for selective photolabeling of proteins and cells. *Science.* 297:1873–1877.

51. Hoyer, M. J., P. J. Chitwood, …, G. K. Voeltz. 2018. A novel class of ER membrane proteins regulates ER-associated endosome fission. *Cell.* 175:254–265.e14.

52. Berg, S., D. Kutra, …, A. Kreshuk. 2019. ilastik: interactive machine learning for (bio)image analysis. *Nat. Methods.* 16:1226–1232. https://doi.org/10.1038/s41592-019-0582-9.

53. MATLAB, 2021. Version 9.11 (R2021b). The MathWorks Inc., Natick, Massachusetts.

54. Leys, C., C. Ley, …, L. Licata. 2013. Detecting outliers: Do not use standard deviation around the mean, use absolute deviation around the median. *J. Exp. Soc. Psychol.* 49:764–766.

55. Weaire, D., and S. Hutzler. 2001. The Physics of Foams. Clarendon Press. https://books.google.com/books?id=mEHlZ9ZodFsC.

56. Lee, C., and L. B. Chen. 1988. Dynamic behavior of endoplasmic reticulum in living cells. *Cell.* 54:37–46.

57. Lu, M., F. W. van Tartwijk, …, C. F. Kaminski. 2020. The structure and global distribution of the endoplasmic reticulum network are actively regulated by lysosomes. *Sci. Adv.* 6, eabc7209.

58. Wilhelm, J., and E. Frey. 2003. Elasticity of stiff polymer networks. *Phys. Rev. Lett.* 91, 108103.

59. Crocker, J. C., and D. G. Grier. 1996. Methods of digital video microscopy for colloidal studies. *J. Colloid Interface Sci.* 179:298–310.

60. Koslover, E. F., C. K. Chan, and J. A. Theriot. 2016. Disentangling random motion and flow in a complex medium. *Biophys. J.* 110:700–709.

61. Schroeder, L. K., A. E. S. Barentine, …, S. Bahmanyar. 2019. Dynamic nanoscale morphology of the ER surveyed by STED microscopy. *J. Cell Biol.* 218:83–96.

62. Weng, T., J. Zhang, …, P. Hui. 2017. Hunting for a moving target on a complex network. *Europhys. Lett.* 119, 48006.

63. Dora, M., and D. Holcman. 2020. Active flow network generates molecular transport by packets: case of the endoplasmic reticulum. *Proc. Biol. Sci.* 287, 20200493.

64. Holcman, D., P. Parutto, …, E. Avezov. 2018. Single particle trajectories reveal active endoplasmic reticulum luminal flow. *Nat. Cell Biol.* 20:1118–1125.

65. Friedman, J. R., B. M. Webster, …, G. K. Voeltz. 2010. ER sliding dynamics and ER–mitochondrial contacts occur on acetylated microtubules. *J. Cell Biol.* 190:363–375.

66. Speckner, K., L. Stadler, and M. Weiss. 2021. Unscrambling exit site patterns on the endoplasmic reticulum as a quenched demixing process. *Biophys. J.* 120:2532–2542.

67. Zucker, B., and M. M. Kozlov. 2022. Mechanism of shaping membrane nanostructures of endoplasmic reticulum. *Proc. Natl. Acad. Sci. USA.* 119, e2116142119.

68. Wang, B., Z. Zhao, …, K. Xu. 2022. The endoplasmic reticulum adopts two distinct tubule forms. *Proc. Natl. Acad. Sci. USA.* 119, e2117559119.

69. Shibata, Y., T. Shemesh, …, T. A. Rapoport. 2010. Mechanisms determining the morphology of the peripheral ER. *Cell.* 143:774–788.

70. Upadhyaya, A., and M. P. Sheetz. 2004. Tension in tubulovesicular networks of Golgi and endoplasmic reticulum membranes. *Biophys. J.* 86:2923–2928.

71. Stadler, L., K. Speckner, and M. Weiss. 2018. Diffusion of exit sites on the endoplasmic reticulum: a random walk on a shivering backbone. *Biophys. J.* 115:1552–1560.

72. Toulmay, A., and W. A. Prinz. 2011. Lipid transfer and signaling at organelle contact sites: the tip of the iceberg. *Curr. Opin. Cell Biol.* 23:458–463.

73. Vecellio Reane, D., R. Rizzuto, and A. Raffaello. 2020. The ER-mitochondria tether at the hub of Ca2+ signaling. *Curr. Opin. Physiol.* 17:261–268.

74. Katona, M., Á. Bartók, …, G. Hajnóczky. 2022. Capture at the ER-mitochondrial contacts licenses IP3 receptors to stimulate local Ca2+ transfer and oxidative metabolism. *Nat. Commun.* 13:6779.

Biophysical Journal, Volume *122*

Supplemental information

Endoplasmic reticulum network heterogeneity guides diffusive transport and kinetics

Zubenelgenubi C. Scott, Katherine Koning, Molly Vanderwerp, Lorna Cohen, Laura M. Westrate, and Elena F. Koslover

S1. SPATIALLY HETEROGENEOUS ACCESSIBILITY OBSERVED FOR MULTIPLE ER STRUCTURES

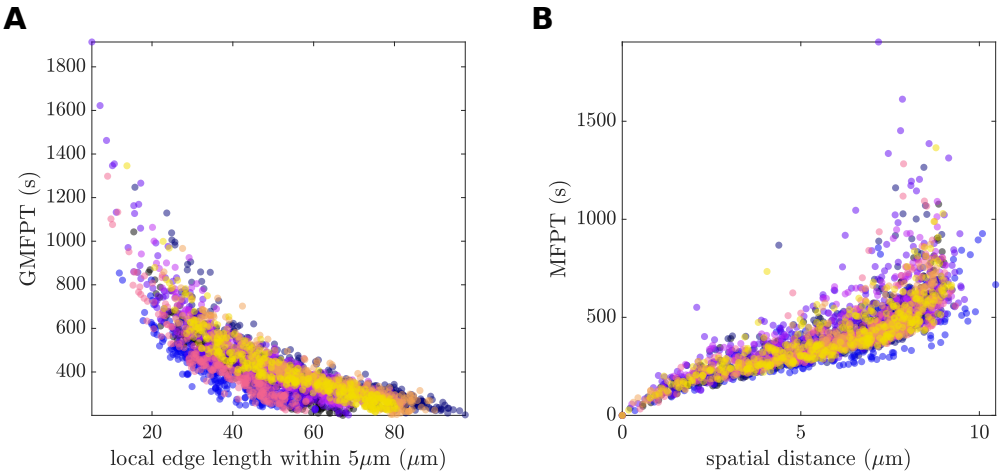

FIG. S1: Diffusive search times for extracted ER network structures. (A) Global mean first passage time (GMFPT) to each node in the network is plotted against the local network edge length (L_{loc}) within $\sigma = 5$ μm of the node. Compare to Fig. 1D. (B) Mean first passage time (MFPT) from a central node to target nodes on the ER network is plotted against Euclidean distance to the target node. Compare to Fig. 1F. In both plots, color indicates results for individual ER architectures (N=8 network regions extracted from 3 cells).

High spatial heterogeneity in network density and diffusive accessibility is observed across multiple excised ER networks. Using eight circular regions (radius 8.5 μm) of extracted ER network structure, local edge lengths and mean first passage times are calculated, as for the example network shown in Fig. 1.

The global mean first passage time (GMFPT) to every node in each network (Fig. S1A) again scales inversely with local edge length. In individual networks, GMFPT can vary by nearly one order of magnitude with similar variation observed in the distributions of local edge length. Notably, the variation within a single network structure is comparable to the overall variation between networks extracted from different cells. Thus, even a well-connected, highly-looped structure like the ER can exhibit large spatial fluctuations in diffusive accessibility, an effect that is observed across multiple peripheral ER architectures.

We next consider a more localized search process wherein a particle begins its search from a central source node (Fig. S1B). The mean first passage time (MFPT) to each possible target node in the ER structures exhibits the characteristic scaling with distance previously discussed in the main text and elsewhere [1]. Fluctuations in ER density and connectivity lead to large deviations from the smooth scaling seen in uniform networks (see Fig. 1E). This implies that in the ER search times for targets that are equidistant from a central source can vary substantially depending on the local geometry.

S2. COMPUTING MEAN FIRST PASSAGE TIMES ON RESERVOIR NETWORKS

Our base model treats regions of the ER as networks of edges connected at point-like junctions. This model assumes that the size of the network junctions is comparable to the tubule width. However, the peripheral ER can also include some sheet-like regions that are substantially larger

than the tubule width [2]. Such peripheral sheet regions would form spatially expanded junctions that could serve as localized traps for diffusing particles. We therefore consider an expansion of our model that incorporates enlarged junction regions from which particles escape through narrow holes along the boundary.

In addition, the perinuclear region of the ER forms a complex structure composed of interconnected stacks of sheets. The detailed structure of the perinuclear ER cannot be resolved with confocal microscopy, but given the large extent of the region we might also expect it to serve as a substantial trap for diffusing particles. A simplified representation of the perinuclear region would also treat it as a disk-shaped reservoir connected to many tubules around its circumference. We use the same mathematical approach to handle the large perinuclear region as we do for the enlarged junction nodes. This approach is described below.

We propose a "reservoir network" model for calculating analytic mean first passage times in a structure composed of tubes that are joined either at point-like nodes or at larger reservoirs. The approximate analytical approach for transitions between reservoirs and tubes is inspired by previous work describing diffusive escape from pores in cylindrical geometries [3].

In essence, the model represents transitions of particles between disk-shaped reservoirs and connecting tubules (Fig. S2A) by decomposing the system into several discrete spatial states (Fig. S2B), in a manner analogous to the classic paper on diffusion-limited reactions by Berg and Purcell [4]. By using a state-based approach, it is then possible to calculate MFPTs on these hybrid reservoir networks using the previously described graph-theoretic approach [5].

In Supplemental Section S3 we apply this model to study the effect of scattered reservoirs on average search times on a network. Additionally, in the main text, a single reservoir representing the sheet-like ER in the perinuclear region is used to more accurately capture search times on a whole-cell scale.

S2A. State diagram for a single reservoir

Reservoirs are treated as disks of radius R_+, with holes in the boundary of width 2δ representing connected tubes (a typical geometry is shown in Fig. S2A with the corresponding state diagram in Fig. S2B). An optional target at the center with radius R_- is denoted the central state, C. When a particle enters the reservoir from an adjoining tube it is placed in the boundary state, B, a distance σ from the outer wall of the reservoir. The value of σ is chosen to be comparable to the tube size, and represents a distance from which the particle can take independent samples of the domain wall without maintaining a strong memory of the tubule from which it came. From state B, the particle can either transition back towards the wall or take the long journey to the center of the reservoir, with splitting probabilities ($\mathcal{E}_\pm$) and average waiting time until the transition (Q_B) given by:

$$\begin{aligned}
\mathcal{E}_+ &= \log\left(\frac{R_+ - \sigma}{R_-}\right) / \log\left(\frac{R_+}{R_-}\right), \\
\mathcal{E}_- &= 1 - \mathcal{E}_+, \\
Q_B &= \frac{1}{4D\log\left(\frac{R_-}{R_+}\right)}\left((R_+ - \sigma)^2 \log\left(\frac{R_+}{R_-}\right) + R_+^2 \log\left(\frac{R_-}{R_+ - \sigma}\right) + R_-^2 \log\left(\frac{R_+ - \sigma}{R_+}\right)\right).
\end{aligned} \tag{S1}$$

Here D is the particle diffusivity, $\mathcal{E}_+$ is the probability of hitting the wall before the central target, and $\mathcal{E}_-$ is the probability of first hitting the central target. If there is no target at the center of the reservoir, then $R_- \to 0$ and $\mathcal{E}_+ = 1$. These expressions are derived from the standard solution of first passage times for the diffusion equation in cylindrical coordinates [6].

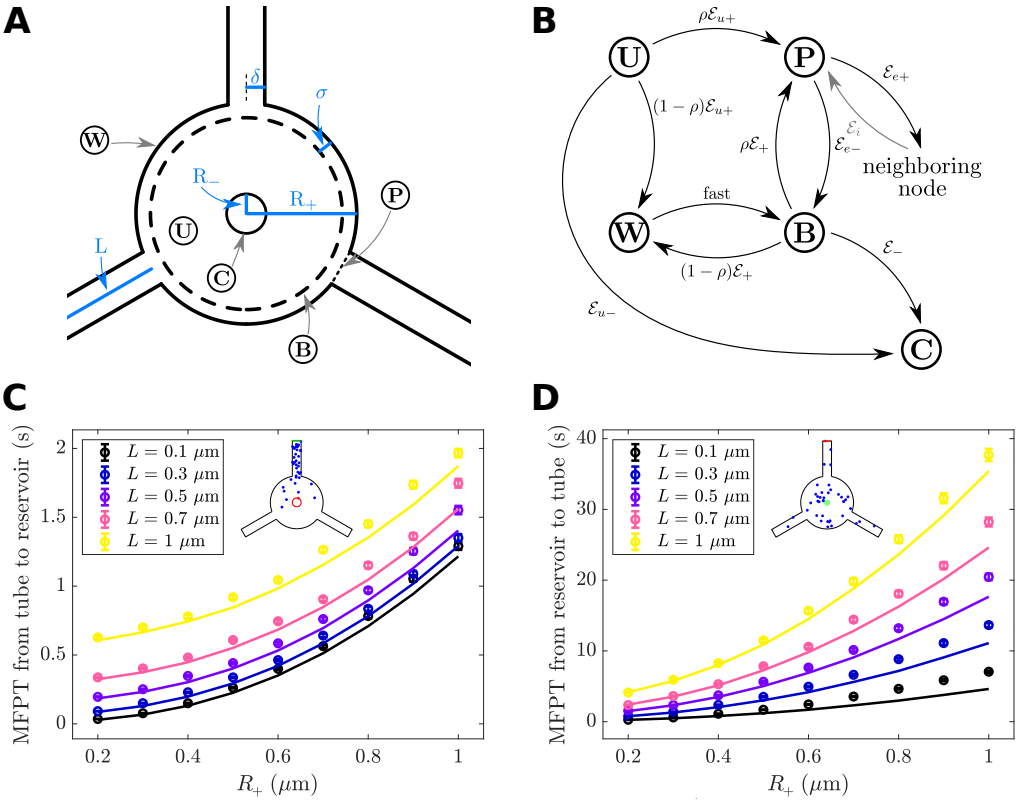

FIG. S2: Reservoir network model. (A) Representative geometry for a three-tube reservoir embedded in the network. Dimensions of the system are highlighted in light blue. The five states and their locations in space are denoted by circled capital letters. (B) The state diagram for the effective model with transition probabilities labeled. The reservoir may be embedded in a larger network, so an additional neighboring node state is depicted where the transition into P from the neighbor is given as in [5]. (C) Analytic MFPTs (lines) reproduce MFPT from BD simulations (points) of 2000 particles diffusing ($D = 1\ \mu\text{m}^2/\text{s}$) across wide range of symmetric triskelion geometries. Error bars show standard error of the mean. Inset: particles (active, blue; absorbed, red) start at the green tip of one tube and diffuse until reaching the red target at the center of the reservoir. (D) Simulations validate the reverse process. Inset: particles start at the center of the reservoir (green) and diffuse until reaching the tip of the top tube (red).

If the particle first hits the wall, it has a chance $\rho = \frac{\delta d}{\pi R_+}$ of entering a P state, where d is the number of tubules connected to the reservoir. The particle is equally likely to hit each P state (this does not mean it will reach the connected node with equal probability, which depends on the length of the intervening edge). The P state can be thought of as a network node connected to two edges: one of length L leading to the neighboring node outside the reservoir and one of length σ leading into the reservoir. The splitting probability from P to B is simply $\mathcal{E}_{e-} = \sigma/(L+\sigma)$. If the particle instead hits the wall, W (probability $1-\rho$), it rapidly transitions back to state B. Assuming σ is small compared to R_+, the waiting time in W will be negligible compared to the time spent performing searches of the bulk. This approach for exit out of a reservoir through a long tube has been previously described for cylindrical geometries [3].

Included in the state diagram is an additional state, U, an optional initial state representing a uniform distribution of particles throughout the reservoir. The splitting probabilities and waiting

times unique to state U are given by:

$$\begin{aligned}\mathcal{E}_{u+} &= \frac{R_+^2}{R_+^2 - R_-^2} + \frac{1}{2\log\left(\frac{R_-}{R_+}\right)},\\ \mathcal{E}_{u-} &= 1 - \mathcal{E}_{u+},\\ Q_U &= \frac{1}{8D}\left(R_-^2 + R_+^2 + \frac{R_-^2 - R_+^2}{\log\left(\frac{R_+}{R_-}\right)}\right).\end{aligned} \tag{S2}$$

For simplicity, this state diagram represents a reservoir with one connected tubule. In practice, there are often multiple P states, each connected to a neighboring node. Then the transitions from U and B to each P_i would be symmetric and scaled by the degree (number of neighbors) of the reservoir.

This reservoir model can be inserted into previously described network models of the ER. Using the splitting probabilities and waiting times for each state, it is possible to calculate analytic mean first passage times for diffusive search in the reservoir as previously described in [5].

S2B. BD simulations in triskelion geometries validate analytic approach

The analytic model is validated through the use of Brownian dynamics simulations on triskelion geometries with a wide range of sizes (Fig. S2C,D insets). The radius of the reservoir, R_+ is varied between $0.2 - 1.0$ μm and the length of the connected tubules is varied from $0.1 - 1.0$ μm. The radius of the tubes is fixed at $\delta = 0.05$ μm, a typical size for ER tubules in COS7 cells [2, 7]. The modified tube size, is set to $\sigma = \pi\delta/4$ as in [3, 4]. In all of these tests (and later applications), the central target has radius $R_- = \delta$ so that targets placed in either a tube or a reservoir have the same size.

Two representative search problems are analyzed on these geometries. In the first test, 2000 particles are placed at the end of a tube and allowed to diffuse until reaching an absorbing disk at the center of the reservoir (Fig. S2C). In the second, 2000 particles begin at the center of the reservoir and diffuse until reaching the end of a specific tube. The time step for both tests is 10^{-5} s, with particle diffusivity $D = 1$ μm^2/s. The MFPT is recorded and compared to the analytic MFPT from the corresponding reservoir network (Fig. S2C,D).

Over a wide range of scales for both R_+ and L the analytic model approximately reproduces simulated mean first passage times. Having validated a single triskelion, it is now possible to intersperse these reservoir structures throughout existing networks and obtain realistic mean first passage times on reservoir networks.

S3. PRESENCE OF SCATTERED RESERVOIRS INCREASES TRAPPING, GMFPT

By treating the peripheral ER as a network of one-dimensional tubules we are able to focus on large-scale structure and connectivity. This enables us to model transport in the ER as diffusion on a network, where simple computational approaches provide powerful predictions that agree with experimental results (Fig. 2E). Here we investigate the limits of the network model by considering the effect of scattering enlarged junction reservoirs over a network.

A COS7 peripheral ER is modeled as a reservoir network by randomly selecting 20% of its nodes and converting them into reservoirs. The reservoir radii (R_+) are set to be 0.45 of the minimum

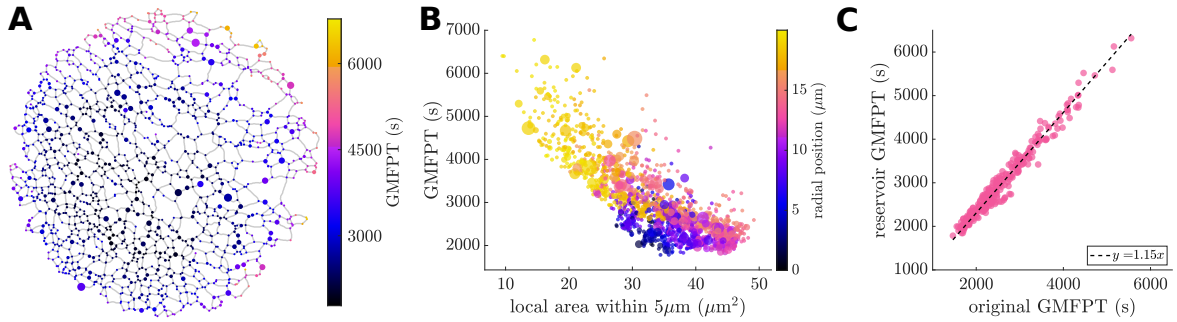

FIG. S3: Reservoir network model of a COS7 ER. (A) Global mean first passage times (GMFPTs) to targets on nodes on an example COS7 ER network (from Fig. 1A) where now 20% of network nodes are converted to reservoirs. Reservoir nodes are shown as true size, point-like nodes are plotted with a fixed minimum size for visibility. (B) GMFPT scales inversely with local network surface area. Color denotes radial position from center of network, enlarged points indicate reservoirs and their relative size. (C) The GMFPT to central targets in reservoirs scales linearly with GMFPT of the original nodes (prior to conversion to reservoir).

edge length connected to the node, giving an average size of 0.26 μm. Connected edges shrink to accommodate the reservoirs. This avoids unphysical overlap of reservoirs and edges and allows for a heterogeneous distribution of reservoirs to be randomly dispersed across the network. The GMFPT is calculated to targets of radius $R_- = 0.05$ μm placed in the center of each expanded node, as well as to all the ordinary point-like junctions. Because the particles are meant to represent ER membrane proteins, the starting probability for each node is set in proportion to surface area, with non-reservoir nodes assigned surface area $2\pi\delta^2$, while reservoirs have surface area $2\pi R_+^2$.

We find that even in the presence of many reservoirs, the qualitative trends for network search times are the same. GMFPT still scales with the amount of locally accessible network (in this case, surface area, Fig. S3B). For each individual reservoir target, we compare its GMFPT in a network with many reservoirs versus the GMFPT to the same node on a network with point-like junctions only (Fig. S3C). The main effect of enlarged junction reservoirs is a slight increase in search times. This is due to the increase in network surface area and the trapping that occurs inside of reservoirs; there is more space for particles to explore before finding any given target and thus average search times increase. Notably, the breadth of the search-time distribution does not change substantially upon the introduction of randomly scattered enlarged reservoirs. Thus, treating the ER tubule junctions as point-like connections appears to be a reasonable simplification for these network structures.

S4. ALTERNATIVE METHODS OF INCORPORATING NETWORK DYNAMICS INTO SIMULATIONS OF PARTICLE DIFFUSION

When modeling the spread of photoactivated diffusing particles from a central region, the dynamic rearrangements of the ER network need to be considered. In the main text, we incorporate the effects of the time-varying ER structure by averaging multiple simulations on static networks extracted from individual frames of the experimental movie. Here, we analyze two alternatives: (1) simulations run only on a single network extracted from the first frame; and (2) a "project and propagate" approach incorporating many network snapshots in each simulation. In both cases, the same two rounds of filtering are applied when comparing to the experimental signal.

For approach (1), the simulated fractional signal on the network extracted from frame 1 (f_{1ij}^{sim}) is plotted in Fig. S4A.ii. We calculate the slope of the signal in each wedge j over the first 10

seconds after photoactivation. These arrival rates are compared to the averaged simulated rates from the main text (computed from the averaged fractional signal shown in Fig. S4A.iii). We see strong agreement between the two ($R^2 = 0.91$, Fig. S4B, blue dots and dashed line). Consequently, this approach also does reasonably well in predicting the experimentally measured protein arrival rates (extracted from Fig. S4A.i), with $R^2 = 0.6$ (Fig, S4C, blue dots and dashed line). Approach 1 includes no information about the network rearrangements over time, but still captures much of the behavior of proteins in the ER.

For the project and propagate simulations, 50000 particles commence diffusion from the photoactivation region on the network extracted from the first frame of the movie. The photoactivated particles then diffuse along the first network for time $dt = 0.6$s, at which point they are projected from their location in space to the closest point on the network extracted from the second frame of the experimental movie. The projection step tends to be small compared to the diffusive (or propagation) step because the network evolves slowly in time compared to the diffusion of individual particles. The diffusive particles repeat this process, propagating and projecting, until the final frame of the experiment is reached.

One advantage of this method is that it more realistically captures the expected spatial trajectories of particles diffusing on a continuously rearranging network. As time progresses and the proteins diffuse from the photoactivation region, the network evolves in time as well, albeit with a large time step set by the experimental frame rate.

The same nine photoactivation runs are analyzed using the project and propagate simulation method. We again define individual wedge regions of the same size and location as in the experimental images and analyze the number of particles in each. The simulated signal in each wedge (w_{ij}^{pp}) is then defined as the total number of particles in wedge j at time point i, and the fractional signal (Fig. S4A.iv) is $f_{ij}^{\mathrm{pp}} = w_{ij}^{\mathrm{pp}}/N$. These fractional signals do not require averaging as in the main text, because the effects of the dynamic network are already incorporated via the project and propagate method. The fractional signals are then used to find the signal arrival rate (slope over first 10 seconds), just as before.

Again, we see strong agreement between the project and propagate simulations and the results from the main text when comparing the calculated arrival rates (Fig. S4B). The project and propagate method is also able to predict the experimental arrival rates well: $R^2 = 0.64$ (Fig. S4C), as compared to $R^2 = 0.68$ in the main text.

Both project and propagate and the frame-averaged approach outlined in the main text generate simulated protein arrival rates that fit the experimental rates slightly better than the static approach using the first frame only. These approaches for incorporating ER network dynamics thus help account for the time-varying tubule density and connectivity within each ER region. Thus, although ER network dynamics are shown to be quite slow, incorporation of the different network structures over time allows for a better representation of observed particle motion.

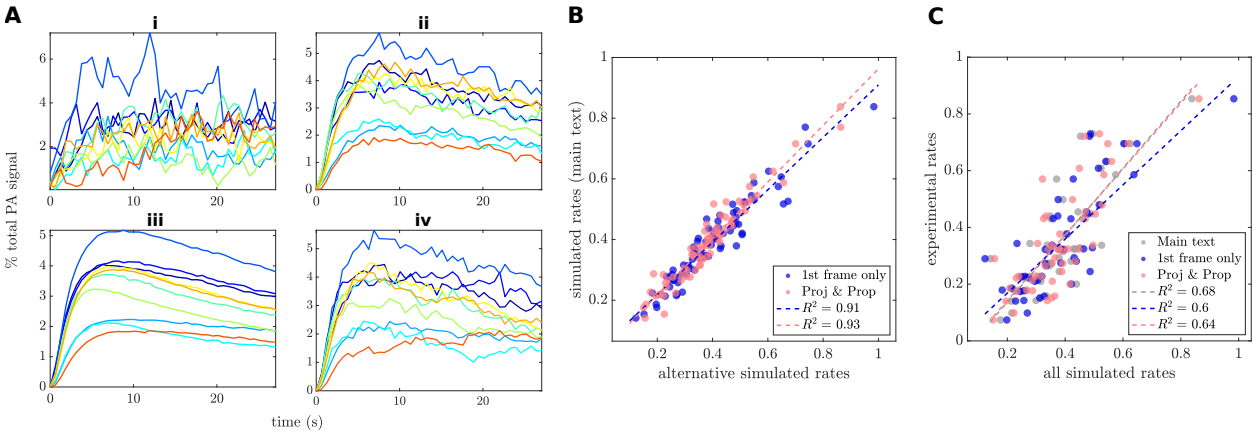

FIG. S4: Alternative simulations of diffusive spread in the ER. (A) Fractional photoactivated signal vs time curves for a single cell from experiment and simulations: (i) experimental signal, (ii) simulated signal on the network from the first frame, (iii) simulated signal averaged over networks from each frame of the experimental movie (as used in main text, Fig. 1E), and (iv) simulated signal from the project and propagate approach. (B) Correlation of signal arrival rates from alternative simulation approaches with the averaging approach used in the main text. (C) Correlations of simulated rates with experimental protein arrival rates.

[1] M. Dora and D. Holcman, Proceedings of the Royal Society B **287**, 20200493 (2020).
[2] L. K. Schroeder, A. E. Barentine, H. Merta, S. Schweighofer, Y. Zhang, D. Baddeley, J. Bewersdorf, and S. Bahmanyar, J Cell Biol **218**, 83 (2019).
[3] Z. Yang and E. F. Koslover, Phys Biol (2023), URL `http://iopscience.iop.org/article/10.1088/1478-3975/acb1ea`.
[4] H. C. Berg and E. M. Purcell, Biophysical journal **20**, 193 (1977).
[5] Z. C. Scott, A. I. Brown, S. S. Mogre, L. M. Westrate, and E. F. Koslover, Eur Phys J E **44**, 1 (2021).
[6] S. Redner, *A Guide to First-Passage Processes* (Cambridge University Press, 2001).
[7] T. Konno, P. Parutto, D. M. Bailey, V. Davì, C. Crapart, M. A. Awadelkareem, C. Hockings, A. Brown, K. M. Xiang, A. Agrawal, et al., bioRxiv (2021).